NOTE TO USERS

DISSERTATION

MEASUREMENTS OF INTERACTIONS OF MEMBRANE PROTEINS

Submitted by

Guy M. Hagen

Department of Chemistry

In partial fulfillment of the requirements

For the Degree of Doctor of Philosophy

Colorado State University

Fort Collins, Colorado

Summer 2005

COLORADO STATE UNIVERSITY

31 MAY, 2005

WE HEREBY RECOMMEND THAT THE DISSERTATION PREPARED UNDER OUR SUPERVISION BY GUY M. HAGEN ENTITLED MEASUREMENTS OF INTERACTIONS OF MEMBRANE PROTEINS BE ACCEPTED AS FULFILLING IN PART REQUIREMENTS FOR THE DEGREE OF DOCTOR OF PHILOSOPHY.

Committee on Graduate Work

Advisor

Department Head

ABSTRACT OF DISSERTATION

MEASUREMENTS OF INTERACTIONS OF MEMBRANE PROTEINS

We have improved upon conventional fluorescence photobleaching recovery (FPR) measurements by introducing two new techniques: total internal reflection interference fringe (TIRIF)-FPR, and high probe intensity (HPI)-FPR. Both of these techniques are designed to enhance diffusion measurements of visible fluorescent protein (VFP)-membrane receptor fusion proteins. TIRIF-FPR restricts photoexcitation to the cell membrane, eliminating contributions to the recovery signal from fluorescent cytoplasmic species. HPI-FPR accomplishes measurements of sparsely-expressed VFP-fusion proteins where conventional measurements fail by increasing laser power in spot-FPR methods. Data with increased fluorescent probe photobleaching in the attenuated measurement beam are thus recorded, and for the first time, correctly evaluated.

We have compared both new and existing FPR techniques on a variety of biological systems including measurements of the mast cell function-associated antigen (MAFA). This regulatory protein is involved in IgE-receptor mediated allergic responses and was also studied using time-resolved phosphorescence anisotropy (TPA) methods. TPA results, which are uniquely sensitive to in-membrane molecular size, indicate the IgE receptor and

the MAFA regulatory protein are linked in the membrane under both resting and activating conditions.

As part of an on-going effort to improve TPA measurements, new strategies for photomultiplier tube (PMT) gating have also been devised. Saturation of the photomultiplier used in TPA measurements during the intense visible laser flash is a serious problem which can cause artifactual signals and damage to the detector. This was previously addressed by rapidly gating the detector off, but artifactual signals arising at the end of the off-gated period persisted. We have thus developed a fast, fully adjustable photomultiplier gate with high extinction that is capable of eliminating the light-induced post gate artifacts encountered with earlier gating techniques.

Guy M. Hagen
Department of Chemistry
Colorado State University
Fort Collins, CO, 80523
Summer, 2005

TABLE OF CONTENTS

LIST OF FIGURES

LIST OF TABLES

CHAPTER 1

BACKGROUND

Beginning in 1970, a series of experiments examining the diffusion of plasma membrane proteins led to the development of an interdisciplinary field examining the biological function and macromolecular dynamics of plasma membrane components. Frye and Edidin[1] labeled membrane proteins of a mouse lymphocyte with fluorescein-derivatized immunoglobulin (IgG). A human lymphocyte was labeled with rhodamine-derivatized IgG. Using Sendai virus, the authors fused the two cells to create a heterokaryon containing both the human and mouse antigens in its plasma membrane. Using fluorescence microscopy and appropriate filter sets for fluorescein and rhodamine, the authors observed that the antigens, initially present separately on each half of the cell, became 90% intermixed after 40 minutes. After repeating the experiment at a lower temperature, and in the presence of reagents known to inhibit protein synthesis, the authors concluded that free diffusion of the antigens in the membrane was the best explanation for the behavior observed. The free diffusion of membrane proteins was also observed earlier by Loor[2], who reported that plant lectins such as concanavalin A caused cell membrane proteins to form patches or "caps" in which large clusters of fluorochrome-labeled membrane proteins were visible. Using reagents that inhibited cellular metabolism, Loor also showed that the process was not passive. Instead it required "active participation of the agglutinated cells themselves."[2] Shortly thereafter,

Singer and Nicolson[3] proposed their "fluid mosaic" model of cell membranes. In this model, a mobile, dynamic mixture of proteins are inserted in a two-dimensional phospholipid bilayer. The authors argued along thermodynamic and biological lines that the membrane was an oriented semi-fluid with only short-range organization. Optical techniques were potentially well-suited for accurate measurements of diffusion of membrane proteins that would be needed to validate the fluid mosaic model.

One of the earliest measurements of lateral diffusion of a membrane protein was that of Poo and Cone[4] who, in 1974, reported on their observations of rhodopsin in frog visual membranes. These authors used a photobleaching method similar to that of Peters[5], who bleached half an erythrocyte in an attempt to measure diffusion of non-specifically labeled membrane proteins. In 1976, Axelrod and coworkers[6] developed a more successful approach to measurement of the lateral diffusion coefficient of membrane proteins which they called fluorescence photobleaching recovery (FPR). This 1976 paper also provided the groundwork for analysis of the recovery of fluorescence after photobleaching of a fluorescent probe. In a typical FPR experiment, an attenuated laser beam was focused onto a fluorochrome-labeled cell membrane as observed in a fluorescence microscope. After recording of initial fluorescence intensity for several seconds using an attenuated laser beam, a few millisecond pulse of laser light intense enough to cause significant photobleaching was applied. The attenuated beam was then used to monitor the diffusion of unbleached fluorophores into the interrogated spot. Analysis of the curve using non-linear curve fitting techniques revealed the diffusion coefficient and fractional mobility of the cell surface protein being observed. Working independently, Jacobson and coworkers[7] developed a similar method, giving it the

name most commonly used today, fluorescence recovery after photobleaching (FRAP). Examples of early successful work with FPR include contributions from Barisas[8], who introduced photobleaching measurements on lymphocytes, and by Ware[9], who examined oligomerization of actin filaments.

Concerns about heating or photodamage from the intense photobleaching pulse were quickly addressed. Axelrod showed via a calculation[10] that a temperature rise of only 30mK could be expected during a typical photobleaching experiment. Jacobson[11] and others showed via electron and light microscopy that cells were not detectably photodamaged by the technique. Concern that the FPR experiment may affect the diffusion coefficient of the fluorescent lipid or protein being examined was resolved in an experiment by Koppel and Sheetz[12]. These authors measured diffusion via FPR and by analysis of fluorescence redistribution after the fusion of two cells. In this technique, a cell on which glycoproteins had been fluorescently labeled was fused with an unlabeled cell. Diffusion of the labeled molecules into the unlabeled membrane was monitored as a function of time. No difference was detected in the diffusion rate or mobile fraction by the two methods, further validating the FPR method.

A paper critical in the development of FPR techniques was that of Saffman and Delbruck in 1975[13]. The authors derived the theoretical expressions for both lateral and rotational Brownian motion of a particle in a membrane. $D(r) = K_bT/4\pi\mu a^2h$; $D(t) = K_bT/4\pi\mu h^*[\text{Log}(\mu h/\mu' a)-\gamma]$ where μ is the viscosity of the membrane(~1 poise), μ' is the viscosity of water(~.01 poise), a is the radius of a membrane protein($\sim 10^{-6}$cm), h is the thickness of the membrane($\sim 10^{-7}$ cm), and γ is Euler's constant (0.5772). This treatment

modified the Stokes-Einstein equation to reflect an environment in which the viscosity of the membrane is much higher than the surrounding water. The lateral diffusion coefficient in such a constrained 2D system has only a logarithmic dependence on molecular size, indicating that FPR measurements yield information about molecular compartmentalization, aggregation, interaction with cytoskeletal elements, and large changes in molecular weight.

Additional improvements to the method continued throughout the 1980s and 1990s. A main difficulty with traditional FPR measurements was the very poor signal-to-noise ratios, especially when attempting the technique on sparsely-expressed cell membrane proteins. Use of patterned photoexcitation, rather than a single spot, increased signal-to-noise ratios significantly. Use of patterned illumination was first developed by McConnell,[14] who used a Ronchi ruling. Barisas and coworkers improved on this by introducing the use of an interferometer which intersected two laser beams in the rear image plane of the photobleaching microscope.[15] This method interrogated the entire cell at once and greatly increased signal levels and thus statistical precision. However, the interference pattern had a great depth of field which precluded its use with highly autofluorescent cells or those cells expressing fusion proteins with green fluorescent protein (GFP) since large contributions to the signal from non-membrane species were encountered. Restriction of photoexcitation to the cell membrane would thus make interferometric FPR possible on such cells.

Total internal reflection (TIR) illumination had been used in fluorescence microscopy for measurements of receptor-ligand interactions[16] and for diffusion measurements via fluorescence correlation spectroscopy,[17] but was rarely utilized in photobleaching recovery experiments.[18,19] Recent development of very high numerical aperture microscope objectives

opened the possibility of through-the-objective TIR illumination.[20] TIR illumination was attractive since only the part of the cell in direct contact with the coverslip, ie, the cell membrane, was excited by the evanescent wave. This completely eliminated contributions to the fluorescence signal from out of plane fluorescence and allows the use of the interferometric technique on cells expressing GFP fusion proteins.

Fusion of GFP to the intercellular terminus of a membrane protein of interest gives a fluorescent marker in cases where reliable antibodies are not available. An example of a membrane protein for which no antibody is available is the receptor for luteinizing hormone (LHR) found on ovarian tissue in mammals. It was, however, possible to evaluate receptor diffusion using a VFP-LHR fusion protein. This dissertation reports for the first time successful integration of interferometric photobleaching recovery measurements on live cells with objective-type TIR illumination and GFP technology.

An alternate way to overcome low signal levels in conventional FPR experiments is to simply increase the power of the exciting laser. This typically caused photobleaching of the fluorescent probe in the attenuated beam. Naive analysis of FPR data that displayed significant photobleaching in the attenuated beam yielded distorted diffusional parameters. Also included in the above study is a refinement of the original spot-FPR technique, which we term high probe intensity (HPI)-FPR. In this method, the probe laser intensity is increased several fold over the nominal 1μW normally used, rapidly photobleaching the sample. By recording data starting with the first instant of attenuated beam illumination, we show for the first time correct analysis of data of this type.

In addition to the studies devoted to FPR method development, this dissertation also

presents a study of a membrane protein important in allergic immunology, the high affinity receptor for IgE, and of its regulatory protein, the Mast Cell Function Associated Antigen (MAFA). Interferometric and spot FPR measurements were conducted for both membrane species under resting and activating conditions. As noted above, the lateral diffusion coefficient has a weak dependence on molecular size[13]. However, measurements of rotational diffusion of membrane proteins are a very sensitive means to determine molecular size *in situ,* since, as mentioned above, the rotational diffusion coefficient is linearly related to the volume of the rotator[13]. To more fully elucidate the functional relationship between the IgE receptor and MAFA, rotation measurements via time-resolved phosphorescence anisotropy (TPA) were also conducted. Time-resolved phosphorescence anisotropy methods for cell membrane protein rotation measurements were introduced by Jovin and coworkers,[21-23] who have also studied the IgE receptor system via anisotropy measurements[24]. In such a measurement, 10^7 cells per ml are labeled with erythrosin-derivatized antibodies specific for the membrane protein of interest. After washing away any unbound probe molecules, the cells are excited by a vertically polarized Q-switched laser. Phosphorescence emission is collected at 90 degrees from the excitation axis through a polarizer oriented parallel, then perpendicular to the vertical excitation pulse. The emission anisotropy is calculated as $r(t) = (I_{\parallel}-I_{\perp})/(I_{\parallel}+2I_{\perp})$. The anisotropy curve is then fitted to $r(t)=r_{\infty} + (r_0-r_{\infty})\exp(-t/\phi)$ where r_0 and r_{∞} are the initial and limiting anisotropy values, and ϕ is the rotational correlation time (RCT). Other methods for rotational diffusion measurements have been reported, notably depletion of polarized fluorescence (PFD). This technique was introduced by Johnson and Garland[25]and can be accomplished on single cells in a microscope. Barisas and coworkers

have utilized the PFD technique in several situations,[26-32] and have expanded the technique using continuous, repetitive excitation waveforms that rely on a single laser.[33]

Time resolved phosphorescence anisotropy and polarized fluorescence depletion measurements require use of an intense pulse of visible light from a Q-switched laser. Detector saturation from the pulse must be avoided as this can cause irregularities in the photomultiplier (PMT) gain characteristics or even damage. Development of PMT gating circuitry to switch the detector off during the laser flash has long been of interest for phosphorescence anisotropy[34-36]applications. In a normally-on photomultiplier, a negative or positive-going voltage pulse can be applied to intermediate dynodes such that the order of potentials in the PMT voltage divider is reversed. Electron amplification is thus made impossible, effectively turning the tube off. An attenuation of at least 10^5 can easily be achieved with this method. Even when gating is employed and light levels are modest, light induced post gate artifacts (LIPGA) occur. Spurious anode signals arising at the end of the gated period are attributed in the literature to bombardment of the photocathode (PC) by positive gaseous ions created in the PC-dynode1 (D1) space. These ions are created by the 80-100eV electrons produced by the laser pulse. If the potential between the PC and dD1 can be held to 10V, no ionization will occur, while still maintaining forward bias in the PMT. This dissertation presents a flexible gating circuit that eliminates afterpulsing via this strategy as part as an ongoing effort to improve the quality of TPA measurements.

Adapted From: B. G. Barisas, D. A. Roess, G. C. de Leon, and G. M. Hagen, *Proc. SPIE*, (2004), 5329, p 44-53.

CHAPTER 2

LATERAL DIFFUSION MEASUREMENTS ON GENETICALLY-INTRODUCED FLUORESCENT PROTEINS

INTRODUCTION

Genetic introduction of fluorescent labels such as the Visible Fluorescent Proteins (VFP) has revolutionized the visualization and characterization of cellular proteins. VFP constructs involving membrane receptors have been particularly important because of the critical roles played by receptors in cellular signaling processes. Lateral diffusion measurements, most commonly accomplished through Fluorescence Photobleaching Recovery (FPR or FRAP), provide important information on such molecules' size, environment and participation in intermolecular interactions including ligand-driven associations.

FPR measurements on VFP-constructs present two particular challenges. First, such membrane receptors are frequently expressed at levels as low as 10,000 per cell. Thus techniques must be employed which deal with the correspondingly low fluorescence signals. Second, cytoplasmic VFP-species invariably accompany membrane receptors. These cytoplasmic molecules contribute to the fluorescence recovery signal and thus distort measurements aimed at surface molecules. Figure 1 illustrates this problem. Although the GFP-epidermal growth factor receptor fusion protein (GFP-erbB1) expressed by these cells

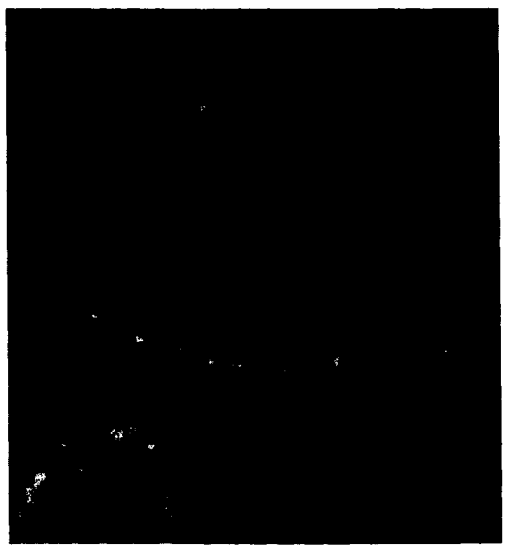

Figure 1: Confocal fluorescence micrograph of GFP-erbB1 on F1-4 CHO cells showing both membrane localization of receptor and cytoplasmic species.

is substantially localized at the cell surface, considerable fluorescent material nonetheless permeates the cytoplasm. A similar circumstance also arises from cellular autofluorescence which frequently appears in non–VFP cell lines. Thus, FPR methods are required which examine cell membrane molecules without interference from cytoplasmic species.

The common method of spot fluorescence photobleaching recovery (spot FPR)[6] using a tightly-focused laser beam is easy to implement and the confocality conferred by the image plane aperture substantially eliminates cytoplasmic fluorescence. However, the fluorescence signal obtainable from a sub-micrometer membrane spot is typically small, especially given low levels of receptor expression, and signal-to-noise ratios of individual fluorescence recovery traces are correspondingly low. Thus, large numbers of individual measurements typically must be averaged to yield acceptable results.

To avoid this difficulty, we previously developed Interference Fringe Fluorescence Photobleaching Recovery (IF-FPR)[37] to permit simultaneous interrogation of a cell's entire surface. In this method, a three-dimensional fringe pattern is generated interferometrically within the optical path of an FPR system by intersecting two laser beams at the rear image plane of the objective. The fringe pattern interrogates the entire cell at once and so affords much increased signal levels and greatly improved reproducibility of measurements. However, the technique intrinsically possesses tremendous depth of field and so collects fluorescence from the entire cell volume. Hence, it is not satisfactory for cells expressing GFP fusion proteins or other cells with high levels of cytoplasmic fluorescence. Total Internal Reflection (TIR)[19] allows selective excitation of fluorophores contacting a glass-water interface since the evanescent wave decays exponentially above the interface with a

decay length on the order of 100nm. The convenience of TIR illumination has been greatly facilitated by development of very high numerical aperture microscope objectives. These objectives allow TIR epi-illumination *through* a microscope objective[20]. Such surface-selective excitation has facilitated, for example, single-molecule imaging[38]. We have now combined objective-type TIR illumination with interferometric fringe generation to selectively measure lateral diffusion of only membrane species on living cells. We term this method Total Internal Reflection Interference Fringe Fluorescence Photobleaching Recovery (TIRIF-FPR).

Spot FPR methods allow a different strategy for improving quality of data obtained. In such experiments investigators frequently increase the intensity of the probe laser beam in an effort to improve signal levels. However, probe beam photobleaching during such measurements distorts the recovery kinetics in complex ways that have, in the past, not fully been appreciated. This distortion makes accurate estimates of the diffusion coefficient and fractional mobility impossible when data are acquired and analyzed by standard techniques[6]. This problem has been encountered recently in a multiphoton-FPR experiment on microinjected spiny dendrites of cerebellar purkinje cells[39], where some data were discarded due to excessive photobleaching in the probe beam. We have now developed a method we term High Probe Intensity Fluorescence Photobleaching Recovery (HPI-FPR) in which we increase the probe beam power up to 10-fold over that typically used. We thus obtain substantially more data per unit time from the illuminated region which remains the same as in spot FPR. This higher probe power causes marked sample photobleaching during recovery. Nonetheless, by acquiring data from the absolute beginning of sample exposure

to the probe beam and analyzing these data as described below, accurate values for diffusional parameters are obtained with precision improved substantially over conventional spot methods.

EXPERIMENTAL METHODS

Materials. Minimal essential medium (MEM), Dulbecco's modified Eagle medium (DMEM) containing high glucose, geneticin, cell culture antibiotic solutions, and fetal bovine serum (FBS) were all purchased from Invitrogen, Carlsbad, CA. Non-essential amino acids were purchased from Sigma Chemical Co., St. Louis, MO. Alexa 488 was purchased from Molecular Probes, Eugene, OR. G63 MAFA-specific mAb was a kind gift of Professor Israel Pecht, Weizmann Institute of Science, Rehovot, Israel.

Cell lines and sample preparation. Chinese hamster ovary (CHO) cells were stably transfected with C-terminal fusion proteins of enhanced GFP with wild type rat luteinizing hormone receptor (GFP-LHR cells)[40], or wild type rat gonadotropin hormone releasing hormone receptor (GFP-GnRHR cells)[41]. These cells were maintained in DMEM with high glucose containing 10% fetal bovine serum (FBS), antibiotics and non-essential amino acids, pH 7.4. This medium was supplemented with 200 μg/mL geneticin to select for cells expressing GFP fusion proteins. CHO cells stably expressing the C-terminal fusions of enhanced GFP with epidermal growth factor receptor (GFP-erbB1 cells)[42] were a kind gift from Dr. Tom Jovin of the Max Planck Institute for Biophysical Chemistry, Göttingen, Germany. These cells were maintained in the medium described above for other CHO cells, except geneticin was omitted from the medium. Rat basophilic leukemia cells of the 2H3 line (2H3 cells) were maintained in MEM supplemented with antibiotics and 15% FBS. All cells

were grown at 100% humidity in 5.5% CO_2 at 37°C. After removal from tissue culture flasks using 5 mM EDTA in PBS, cells were pelleted at 300 times the force of gravity (300x g) and re-suspended in PBS. In some experiments, 2H3 cells were labeled with Alexa 488 conjugates of G63 Fab as described previously[43]. Cells were placed on quartz well slides, overlaid with No. 1.5 Pyrex or SF-11 coverslips and then inverted on the microscope. No fixation or mounting agents were used and measurements were performed at room temperature.

Fluorescence photobleaching recovery measurements. The optical system for fluorescence photobleaching recovery measurements has been described in detail[37]. The inverted Zeiss Axiomat microscope used in this study was equipped with a Zeiss 63x Plan Neofluar water immersion objective, NA 1.2, and, for TIR interference fringe photobleaching measurements, an Olympus 100x Apo objective, NA 1.65. Special high refractive index coverslips (type SF-11, VA Optical Labs, San Anselmo, CA) and immersion fluid were required for the Olympus objective. An attenuated Coherent Radiation Innova 100 argon ion laser operating at 488 nm was focused to a spot of 0.38μm e^{-2} radius and a standard Zeiss FITC-selective filter set was used for both Alexa 488 and GFP fluorophores. In conventional spot photobleaching measurements, bleaching beam power was typically 6 mW. For HPI spot measurements, powers were approximately 5- to 10-fold higher. The ratio of intensities in the bleaching and probe beams was held constant at about 3000 and was measured carefully for HPI measurements. A confocal image plane photometer aperture was used in both conventional spot and HPI spot measurements to eliminate out-of-plane fluorescence. HPI spot measurements required that the sample be illuminated with the probe laser beam only

during data acquisition. To permit accurate focusing on the sample, a 3 mW 635 nm diode laser (Coherent Auburn Division, Auburn, CA) was aligned co-linear with the optical axis. Objective focus at the level of the cell membrane was detected by the appearance of a sharp spot of scattered red light. This laser was turned off at the beginning of data acquisition. For all experiments, data were acquired at 50 msec/point for 20 sec before and for 25 sec after the bleaching pulse, and were processed off-line with a Marquardt nonlinear curve fitting program developed for this application. Conventional spot photobleaching data were analyzed assuming no bleaching by the probe beam while HPI spot data were analyzed to allow a non-zero rate of probe bleaching. In some instances, the ratio of bleach and probe intensities and the length of the bleach pulse were input into the fitting procedure to fix the relation between the rate of probe bleaching and the extent of bleaching by the bleaching pulse. This strategy reduced the number of fitted quantities by one and, hence, improved the precision of other fitted parameters. For curve fitting purposes, fluorescence recovery curves were calculated either from the series solution, or from direct numerical simulation, of the bleaching-diffusion equation as described below. Analysis of each recovery trace yielded the initial fluorescence intensity, the rate constant for bleaching in the probe beam (set to zero for conventional spot data), the extent K of bleaching in the bleach pulse[6], the diffusion coefficient and the fraction of fluorescent molecules mobile on the experimental timescale, as well as linear estimates of uncertainties in these quantities.

For conventional interference fringe FPR measurements, an interferometer inserted in the beam path[37] divided the laser beam into two equal-intensity components which intersected at an angle of a few degrees in the external image plane of the microscope's epi-illumination

port. The resulting three-dimensional fringe pattern was directed through the center of the objective back focal plane and imaged onto the sample over an illuminated region of 10 - 20 μm e^{-2} radius. For various interference fringe photobleaching measurements, the fringe spacing ranged from 1.26 μm to 3.65 μm as measured by a CCD camera. A spatial filter improved the quality of the TEM00 laser beam and significantly improved the modulation of the fringe pattern at the sample. To achieve objective-type TIR illumination with the Olympus 100x objective, the interfering laser beams were steered to the periphery of the objective back focal plane where the NA exceeded 1.38 (see Figure 2). Figure 3 illustrates the TIR interference pattern illuminating a GFP-LHR cell. In all interference fringe FPR experiments, the photometer acceptance region was set large enough to encompass the entire cell. Fringe photobleaching data were analyzed as previously described[37], assuming spherical and planar illuminated cell regions in conventional fringe and TIR fringe experiments, respectively.

THEORY UNDERLYING ANALYSIS OF HPI-FPR DATA

Efficient calculation of diffusion accompanied by continuous bleaching is not a trivial problem. The corresponding differential equation does not represent a standard problem in heat conduction and so has not benefitted from the extensive attention historically accorded such topics. For isotropic diffusion of a single species accompanied by bleaching by a radially-symmetric beam, the equation is

$$D\nabla^2 c(r,t) - BI(r,t)c(r,t) = \frac{\partial c(r,t)}{\partial t} \qquad (1)$$

where c=c (r,t) is the fluorophore concentration, D is the diffusion coefficient, I=I(r,t) is the light intensity and B is the rate-constant for bleaching by light of unit intensity. Assuming the

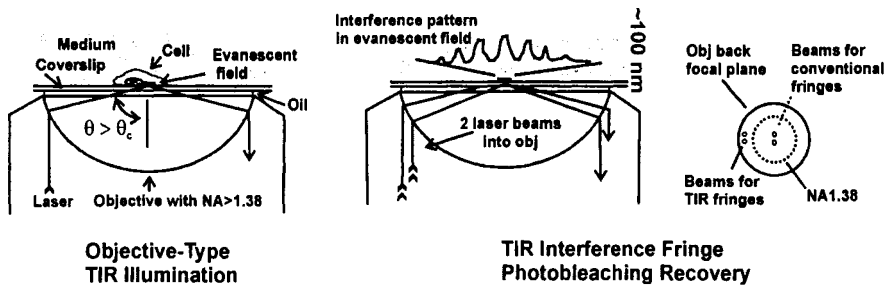

Figure 2: Generation of interference fringes for total internal reflection illumination. Laser alignment is facilitated by the high numerical aperture of the Olympus 1.65N. A. objective. Beam positioning is more critical with lower N. A. objectives.

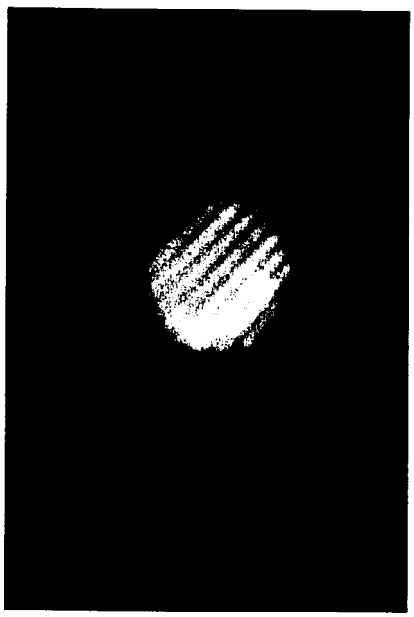

Figure 3: TIR fringes illuminating a CHO cell expressing GFP-LHR. The fringe spacing is 1.46 μm.

light beam to possess a constant Gaussian radial profile, we may replace I(r,t) with $\exp(-a^2r^2)$ I(t) and rearrange equation (1) to read

$$D\nabla^2 c - \frac{\partial c}{\partial t} = Be^{-a^2r^2} I(t)c \tag{2}$$

Calculation of probe bleaching effects on Gaussian spot photobleaching data can be approached on several levels. We consider various strategies with differing ranges of applicability and levels of sophistication.

Case 1: Small extents of probe and pulse bleaching in a Gaussian spot

Consider first a sample examined in a probe beam of constant peak intensity I_p where the ongoing rate of bleaching is small, *i.e.* that $BI_p<<1$, and where a brief pulse of high peak intensity I_b quickly bleaches a small "crater" in the sample. We can, without loss of generality, replace c with $1-c_b$ where $c_b=c_b(r,t)$ represents the fraction of irreversible photobleaching at any instant. Then, in the absence of a bleaching pulse and since the extent of bleaching is small, equation (2) becomes

$$-D\nabla^2 c_b + \frac{\partial c_b}{\partial t} = Be^{-a^2r^2} I_p(1-c_b) \tag{3}$$

We insist that c_b and $\exp(-a^2r^2)$ can both be represented by Bessel Fourier expansions.

$$\begin{aligned} c_b(r,t) &= \int_{k=0}^{\infty} a_k(t) J_0(kr) k dk \\ e^{-a^2r} &= \int_{k=0}^{\infty} \left(\frac{1}{2a^2} e^{-k^2/4a^2}\right) J_0(kr) k dk \end{aligned} \tag{4}$$

Inserting these expressions into equation (3) we obtain

$$Dk^2 a_k(t) + \frac{da_k(t)}{dt} = \frac{BI_p}{2a^2} e^{-k^2/4a^2} \tag{5}$$

Then, observing that $a_k(0)=0$, the solution of equation (5) can be written by inspection as

$$a_k(t) = \frac{BI_p}{2Da^2k^2} e^{-k^2/4a^2} \left(1 - e^{-k^2Dt}\right) \tag{6}$$

While an analytical expression for the actual fluorophore distribution is difficult to obtain, we can nonetheless immediately obtain the time-dependent normalized fluorescence *signal* ΔF as

$$\begin{aligned}
\Delta F / F(0) &= 2a^2 \int_{r=0}^{\infty} c_b(r,t) e^{-a^2 r^2} I_p r dr \\
&= \frac{BI_p}{D} \int_{k=0}^{\infty} \frac{1}{k^2} e^{-k^2/4a^2} \left(1 - e^{-k^2 Dt}\right) \left(\int_{r=0}^{\infty} e^{-a^2 r^2} J_0(kr) r dr \right) k dk \\
&= \frac{BI_p}{D} \int_{k=0}^{\infty} \frac{1}{k^2} e^{-k^2/4a^2} \left(1 - e^{-k^2 Dt}\right) \left(\frac{1}{2a^2} e^{-k^2/4a^2} \right) k dk \\
&= \frac{BI_p}{2a^2 D} \int_{k=0}^{\infty} e^{-k^2/2a^2} \left(1 - e^{-k^2 Dt}\right) \frac{dk}{k}
\end{aligned} \tag{7}$$

Now we substitute z for $k^2/2a^2$ and t' for $2a^2Dt$ to obtain

$$\begin{aligned}
\Delta F / F(0) &= -\frac{BI_p}{4a^2 D} \int_{z=0}^{\infty} e^{-z} \left(1 - e^{-zt'}\right) \frac{dz}{z} \\
&= -\frac{BI_p}{4a^2 D} \sum_{n=1}^{\infty} \frac{(-1)^{n-1} t^n}{n!} \int_{z=0}^{\infty} z^{n-1} e^{-z} dz \\
&= -\frac{BI_p}{4a^2 D} \sum_{n=1}^{\infty} \frac{(-1)^{n-1} t'^n}{n} \\
&= -\frac{BI_p}{4a^2 D} \ell n(1 + t')
\end{aligned} \tag{8}$$

A Gaussian beam profile is most commonly expressed in terms of the $1/e^2$ radius $r_0 = 2^{1/2}/a$ and this gives rise to a characteristic half-time for fluorescence recovery $t_{1/2} = r_0^2/4D$. When these quantities are used to expand a and t', we obtain

$$\Delta F / F(0) = -\frac{BI_p t_{1/2}}{2} \ell n\left(1 + t / t_{1/2}\right) \tag{9}$$

Equation (9) provides a convenient closed-form approximation of the evolution of fluorescence signals during bleaching from the probe beam. Because the extent of any such bleaching is assumed to be small, the recovery of a fluorescence signal after a brief bleaching

pulse of intensity I_b and duration Δt and occurring at a time t_b after initial exposure of the sample to light, can, as a first-order approximation, be calculated independently. For derivation of this recovery, see, for example, Axelrod *et al.*[6]. The final result becomes

$$\begin{aligned} F/F(0) &= 1 - \frac{BI_p t_{1/2}}{2} \ell n\left(1 + t/t_{1/2}\right) \qquad (t < t_b) \\ &= 1 - \frac{BI_p t_{1/2}}{2} \ell n\left(1 + t/t_{1/2}\right) \\ &\quad - \frac{BI_b \Delta t}{2} \frac{1}{1 + (t - t_b)/t_{1/2}} \qquad (t \geq t_b) \end{aligned} \tag{10}$$

Case 2: Arbitrary amounts of bleaching from a Gaussian beam

We assert the existence of a power series solution in B for the inhomogeneous partial differential equation, equation (2)[44]. Without loss of generality, the first term of this series may be taken to be unity. Further, B can be arbitrarily partitioned into the product of two constants B' and B", either of which may be taken to be the power series variable.

$$\begin{aligned} c &= 1 + \sum_{n=1}^{\infty} B^n c_n' \\ &= 1 + \sum_{n=1}^{\infty} (B'B'')^n c_n' \end{aligned} \tag{11}$$

Equating like powers of B', and then setting B" equal to B, we obtain a series of functions

$$c = 1 + \sum_{n=1}^{\infty} c_n \tag{12}$$

for which the recursion relation is

$$D\nabla^2 c_n - \frac{\partial c_n}{\partial t} = e^{-a^2 r^2} BI(t) c_{n-1} \tag{13}$$

The c in equation (12) then converges for all B I(t). We assert that each c_n exists as a Bessel Fourier transform:

$$c_n = \int_{k=0}^{\infty} a_k(t) J_0(kr) k dk \tag{14}$$

Since Bessel functions are eigenfunctions of the Laplacian in radial coordinates, we combine equations (13) and (14) to obtain.

$$\begin{aligned} & -k^2 D a_n(k,t) - \frac{da_n(k,t)}{dt} \\ & = \int_{r=0}^{\infty} BI(t)\left[e^{-r^2} \int_{\ell=0}^{\infty} a_{n-1}(\ell,t) J_0(lr) l dl \right] J_0(kr) r dr \\ & = \int_{l=0}^{\infty} BI(t) a_{n-1}(l,t) \left[\int_{r=0}^{\infty} e^{-r^2} J_0(kr) J_0(lr) r dr \right] l dl \\ & = b(k,t) \end{aligned} \tag{15}$$

where

$$b(k,t) = \frac{BI(t)}{2a^2} \int_{l=0}^{\infty} a_{n-1}(l,t) e^{-\frac{k^2+l^2}{4a^2}} I_0\left(\frac{kl}{2a^2}\right) l dl \tag{16}$$

Evaluation of the inner integral in (15) is per Gradshteyn and Ryzhik 6-633.2[45]. The right-hand side of (15) is thus an explicit function of t, namely through the coefficients $a_{n-1}(k,t)$ comprising the previous term. The inhomogeneous first-order differential equation can be solved explicitly[46] and, if the initial condition is taken to be that c=1 at t=0, then we obtain

$$a_n(k,t) = e^{-k^2 D t} \int_{t'=0}^{t} e^{k^2 D t'} b(k,t') dt' \tag{17}$$

In the more general case, a distribution of diffusion coefficients D_i having fractions f_i, respectively, will be observed. In either case, we may write

$$s(k,t) = \sum_i f_i e^{-k^2 D_i t} \tag{18}$$

Then equation (18) can be re-written as a convolution

$$\begin{aligned} a_n(k,t) &= \int_{t'=0}^{t} s(k,t-t') b_n(k,t') dt' \\ &= s(k) \otimes b(k) \end{aligned} \tag{19}$$

The preceding equation allows the fluorophore distribution function c to be evaluated for any beam intensity varying arbitrarily with time and for any diffusion constant distribution. For computational purposes, the integration indicated in Equation (16) can be conveniently

accomplished by multiplying a vector containing the a_{n-1} by a suitable matrix. A Fast Fourier Transform-based convolution allows equation (19) to be evaluated efficiently and this overall strategy affords a particularly efficient approach to describing diffusive behavior in kinetically-heterogenous systems. Depending upon the diffusion constant, probe bleaching rate and extent of bleaching in the bleaching pulse, various number of terms in equation (12) may be needed to achieve satisfactory series convergence. We typically begin with eight such terms and adjust this number as needed. Once the fluorophore concentration is evaluated, the experimental fluorescence signal F(t) is easily calculated as

$$F(t) = \frac{F_0}{2a^2} \int_{r=0}^{\infty} e^{-a^2 r^2} I(t) c(r,t) r dr \qquad (20)$$

A slightly different strategy for calculating diffusion coupled to continuous bleaching in beams of a uniform circular profile has also been developed based on Laplace transforms and will be published separately.

Case 3: Arbitrary extents of bleaching and arbitrary beam profiles

Closed-form expressions like those described above can be devised for arbitrary extents of bleaching in beams of various profiles. Such expressions, as will be seen below for equation 10, are valuable aids to understanding the underlying physical reality of a given photobleaching experiment. However, these closed-form solutions can be quite complex and each is devised for a particular beam profile. Thus we found direct simulation of the coupled bleaching and diffusion equation, *i.e.* equation (1) for radial coordinates, useful in actual data analysis. An optimized numerical solution of this equation in various coordinate systems[44] was used to simulate the time-evolution of fluorescence recovery kinetics within a special-purpose Marquardt nonlinear fitting program. This allowed fluorescence traces obtained in

spot, fringe and other FPR bleaching geometries and involving arbitrary extents of probe bleaching to be conveniently analyzed.

RESULTS AND DISCUSSION

The TIR interference fringe FPR method provides accurate diffusion measurements on sparsely-expressed membrane species even in cases where conventional interference fringe FPR measurements fail because of cytoplasmic fluorescence

Figure 4 illustrates a comparison of conventional interference fringe and TIR interference fringe FPR measurements of GFP-GnRHR diffusion on transfected CHO cells under comparable conditions. In these cells, the TIR technique provides about one-third the signal of whole-cell conventional interference fringe FPR. Since the TIR measurement cannot include signal from fluorescent cytoplasmic species, these data suggest that as much as one-third the signal observed in the conventional fringe measurement experiments may arise from the cytoplasm. Table I, which shows the diffusion parameters obtained by analysis of spot, conventional interference fringe and TIR interference fringe FPR traces, bears this out. Diffusion coefficients and fractional mobilities via spot and TIR interference fringe methods were measured at 5.4±3.6 and 1.1±0.6x10^{-10} cm^2s^{-1} and 53±22% and 76±23% for the two methods, respectively. By contrast, conventional interference fringe data yield a somewhat higher diffusion constant (6.4±3.3x10^{-10} cm^2s^{-1}) and fractional mobility increased by almost 20% to 94±7%. TIRIF-FPR results are intrinsically free from signal from freely diffusing fluorescent cytoplasmic species, and might be expected to yield a somewhat lower diffusion coefficient than observed with either spot or conventional fringe measurements. This is indeed observed for GFP-GnRHR, as well as in other cases examined. In the case of spot-

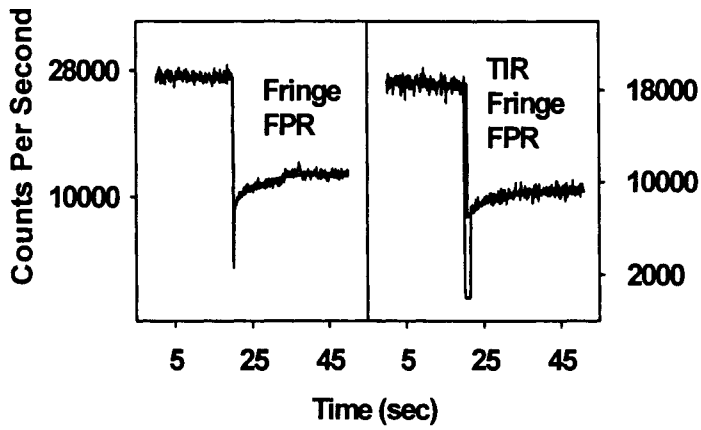

Figure 4: Comparison of conventional fringe and TIR fringe FPR traces of GFP-GnRHR diffusion on transfected CHO cells at 25°C. The TIR technique provides about one-third of the fluorescence signal of whole-cell IF-FPR but rejects all contribution from cytoplasmic fluorescent species.

Method	Avg Signal (CPS)	D (cm^2s^{-1})	M (%)	n
Spot	1,900±700	$5.4\pm3.6x10^{-10}$	53±22%	20
TIRIF	22,000±25,000	$1.1\pm0.6x10^{-10}$	76±23%	12
Conv IF	28,000±10,000	$6.4\pm3.3x10^{-10}$	94±7%	5

Table 1: Diffusion parameters for GFP-GnRHR on transfected CHO cells as evaluated from spot, conventional interference fringe and TIR interference fringe FPR data. Cytoplasmic fluorescence contributing to conventional IF signals renders this technique unsuitable here.

FPR, the degree of confocality gained by the use of an adjustable image plane pinhole, as is commonly employed, may not be as great as desired. Even small contributions to the recovery signal from fluorescent cytoplasmic species may distort spot-FPR results. One might thus expect a higher diffusion coefficient to be measured by spot-FPR than by TIRIF-FPR, as observed for GFP-GnRHR.

As another example of complications caused by cytoplasmic fluorescence in conventional IF-FPR measurements, for GFP-erbB1on F1-4 CHO cells, diffusion coefficients of 5.8±8.3, 2.5±3.0 and 4.7±1.9x$10^{-10}$$cm^2sec^{-1}$ were measured by conventional spot, TIR interference fringe and conventional interference fringe FPR, respectively, while mobilities were estimated at 50±18%, 48±27% and 79±14% for 16, 9 and 8 independent measurements, respectively. Again, TIRIF-FPR results indicate a somewhat lower diffusion coefficient than either spot or conventional interference fringe FPR. Also, mobilities measured by IF-FPR were approximately 20% higher. These diffusion coefficients are substantially slower than published values for GFP-erbB1 diffusion as measured by fluorescence correlation spectroscopy (FCS). In that study[47] the slow component of membrane receptor diffusion was estimated at 1.6x$10^{-9}$$cm^2sec^{-1}$. However, since the optical system used for FCS studies is essentially identical to that used for spot-FPR, it is reasonable to assume that at least some fluorescent cytoplasmic species contribute to the FCS results. Conventional interference fringe FPR results on GFP-proteins again seem discordant with results obtained by other techniques. The mobile fraction appears unreasonably large, a trend observed in most GFP-expressing cells examined to date. By contrast, the surface-selective TIR interference fringe method yields acceptable values for both diffusion and mobility.

Diffusion parameters for GFP-LHR are indistinguishable whether measured on the cell's apical or basal surface.

Since diffusion in TIRIF-FPR experiments is measured at the cell membrane-coverslip contact, it is important to establish whether such contact affects diffusion of membrane species. To do this, we compared using spot-FPR the diffusion and mobility of GFP-LHR on cells in the region of cell membrane-coverslip contact (the basal surface) versus diffusion on the surface facing the medium (the apical surface). Diffusion coefficients of 2.8±3.1 and 2.9±2.6x10^{-10}cm^{2}sec^{-1} and mobilities of 47±24% and 53±15% (n=20, 22) were measured for the basal and apical surfaces, respectively. These quantities are statistically indistinguishable and suggest that membrane contact with the coverslip has little effect on diffusion of surface species.

Even small amounts of sample bleaching in the probe beam can invalidate diffusion parameters obtained by conventional FPR methods

Figure 5 simulates a spot photobleaching recovery trace as typically recorded for a membrane protein on a single cell. This trace illustrates the consequences of increasing FPR probe beam intensity in an effort to increase fluorescence signal. Equation (10) was used to simulate behavior of a protein with a diffusion coefficient (D) of 1x10^{-10}cm^{2}sec^{-}1 and mobility (M) of 100% in a probe beam which bleaches at a rate of 10^{-3} sec^{-1}. As seen in the Figure, these data *appear* to be more-or-less satisfactorily fitted by a conventional $(1+t/t_{1/2})^{-1}$ recovery kinetics model[6]. However, the recovered parameters bear little relation to those which generated the data. The diffusion coefficient is recovered as 1.7x10^{-10}cm^{2}sec^{-1} or 70% high while the mobility is estimated as only 75% or 25% too low. These concerns apply

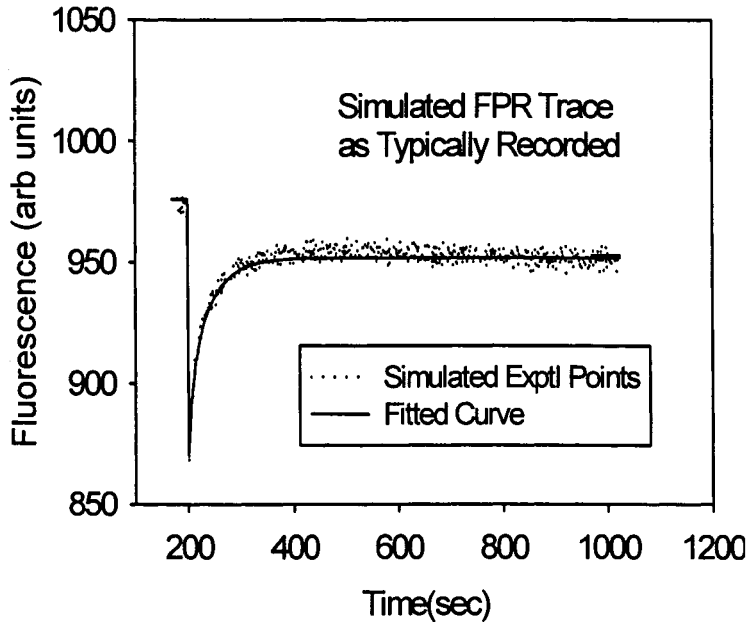

Figure 5: Simulated photobleaching recovery data as typically recorded for a single cell. The sample has been exposed to the probe beam for a substantial time before data are obtained. Naive analysis of these data (smooth curve) yields grossly inaccurate diffusion parameters (see text).

equally to data obtained by spot or fringe techniques; the only determining factor being the intensity of the probe beam to which the sample is exposed.

Obtaining accurate diffusion parameters from spot FPR requires either that the probe beam intensity be very low or that data be obtained from the instant of cell exposure to the probe beam

The reason for the previously-described discrepancy becomes apparent upon inspection of Figure 6. This plot shows the full theoretical curve giving rise to the simulated experimental data in Figure 5. As is typical in such experiments, the sample has been exposed to the probe beam for a substantial but indeterminate time before experimental data are recorded and thus the rate and extent of sample bleaching in the probe beam are never apparent. It is the magnitude of this ongoing bleaching which invalidates the calculated results. Naturally, such bleaching can be avoided by use of extremely low probe beam intensities, approximately 1μW nominal power. However, such intensities rarely yield satisfactory data, especially with sparsely-expressed membrane proteins. However, if data are taken from the instant of cell encounter with the probe beam (Figure 6) and analyzed properly, then the parent diffusion parameters can be accurately recovered. This type of data, which includes points beginning at the initial cell exposure to the probe beam, can only be obtained using some special technique to identify, align and focus on the cell. We use transmitted light to identify cells and a low-power 635 nm diode laser co-linear with the argon laser probe beam to align cells in the laser beam and to focus the beam on one or another membrane. This figure also shows why data analysis must be based on a model properly describing probe bleaching. Such bleaching causes sample fluorescence to decrease with time in complicated

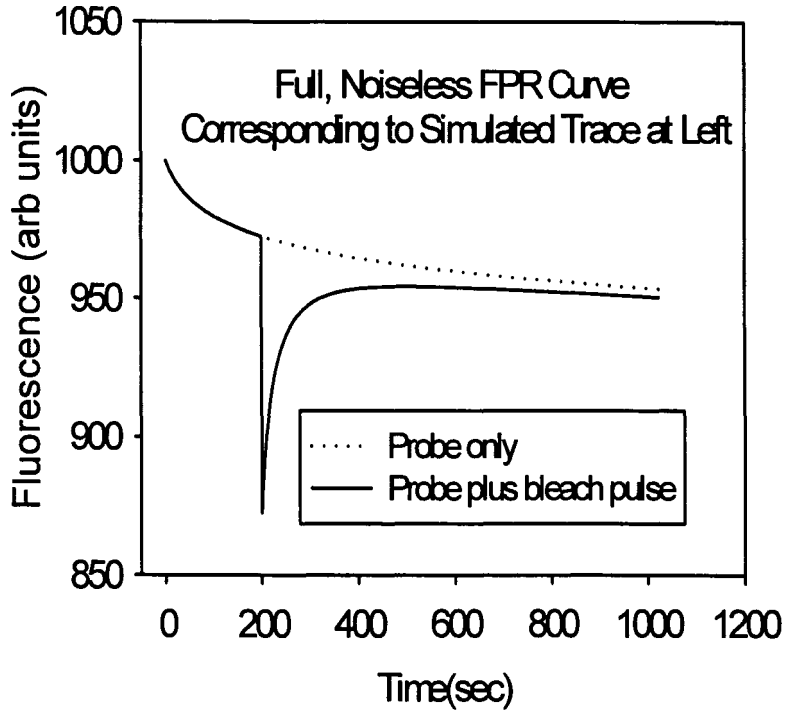

Figure 6: Full theoretical curve (Eq. 10) corresponding to simulated experimental curve in Figure 5. The substantial sample bleaching in the probe beam is only apparent when data are acquired from the beginning of cell exposure to this beam.

logarithmic fashion (equation 10) so that the "baseline" to which fluorescence recovers never becomes level or even linear.

High probe intensity-FPR measurements yield accurate diffusion parameters with precision improved over conventional spot FPR methods

Figure 7 compares conventional and high probe intensity fluorescence recovery curves for GFP-LHR expressed on CHO cells. The probe intensity used in the conventional trace was selected to give no *apparent* bleaching over several recovery half times while the probe beam in the HPI experiment caused approximately 50% bleaching over this period. Analysis of the traces gives diffusion parameters with reasonable agreement, yielding values of 8.7 and $5.1 \times 10^{-10} cm^2 sec^{-1}$ for the conventional and HPI traces, respectively. Mobilities were estimated at 47% for both the conventional and HPI methods. This agreement demonstrates that the experimental and data analysis techniques described previously satisfactorily deal with large extents of probe bleaching. Thus much larger signals can be obtained using HPI methods, in this instance, approximately 7-fold larger than that obtained in the conventional experiment. Hence the statistical uncertainty in measured diffusion parameters is improved over 2-fold by the HPI approach.

HPI-FPR and TIRIF-FPR are applicable to membrane proteins bearing antibody or hormone labels as well as to VFP fusion proteins.

The enhanced FPR methods described above are applicable to any fluorescent cell surface species and will be useful whenever receptor expression is sparse and/or when cells exhibit *any* type of cytoplasmic fluorescence. One example of such a situation is the MAFA regulatory protein[43] of 2H3 cells which occurs in only 20,000 copies per cell. Figure 8 shows

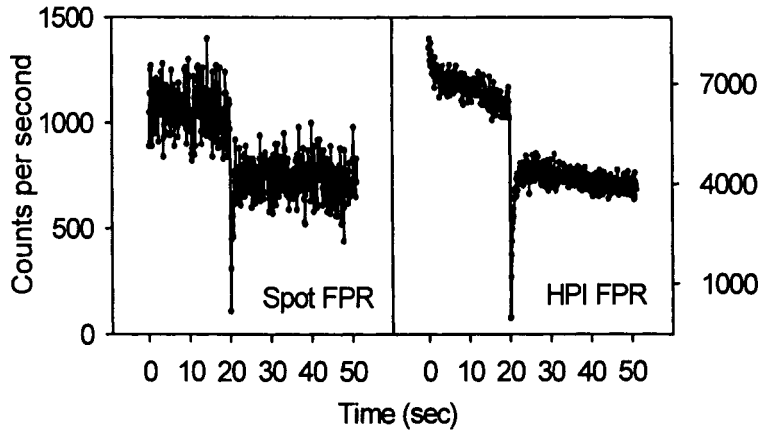

Figure 7: Comparison of conventional spot and HPI spot photobleaching recovery measurements of GFP-LHR lateral diffusion on CHO cells at 25°C. The HPI measurements affords 7-fold increased signal and hence over 2-fold improved statistical precision.

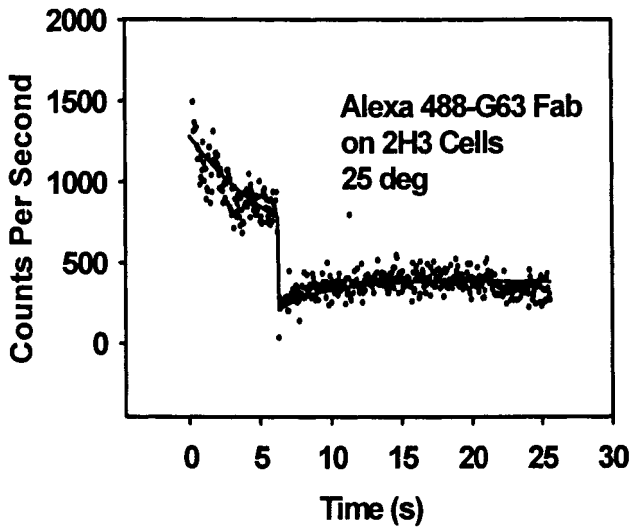

Figure 8: Successful measurement by HPI-FPR of lateral diffusion of the sparsely-expressed MAFA protein on 2H3 cells.

successful measurement of MAFA diffusion on these cells by means of HPI spot photobleaching measurements using Alexa 488-G63 MAFA-specific Fab probe. Previous attempts to measure this diffusion by conventional spot FPR proved unsuccessful owing to low fluorescence signals. Analysis of the HPI data shown yields a diffusion constant of $1.7x10^{-11}cm^2sec^{-1}$ and a fractional mobility of 80%. Although not in good agreement with published results[43] determined by interference fringe methods, the extremely low expression level of MAFA, and correspondingly low signal levels in FPR measurements, leads to a higher degree of uncertainty in the results. Substantial cell-to-cell variability was also noticed in the HPI-FPR experiments on MAFA (not shown).

CONCLUSIONS

We report here two advances in fluorescence photobleaching recovery techniques for measuring membrane molecule diffusion on living cells. These techniques both address problems arising from low levels of receptor expression and from fluorescent cytoplasmic species. Hence they are particularly well suited to examining membrane dynamics of VFP-fusion proteins. TIR interference fringe FPR eliminates interference from cytoplasmic fluorescence while interrogating a substantial fraction of the cell surface. HPI spot FPR maintains the confocality of conventional spot measurements but allows many-fold enhanced signals to be obtained. The consistently lower diffusion coefficients measured by TIRIF-FPR for GFP-fusion protiens suggests that, for such samples, signals in spot methods may not be restricted to the cell membrane to the extent expected. An important contribution of improved precision in such measurements is the possible identification of cell-to-cell

variation in biophysical parameters currently obscured by the poor reproducibility of diffusion data.

ACKNOWLEDGMENTS

The Author is grateful to Dr. Tom Jovin, Max Planck Institute for Biophysical Chemistry, Göttingen, Germany, for making available the F1-4 CHO cell line expressing GFP-erbB1 and to Prof. Professor Israel Pecht, Weizmann Institute of Science, Rehovot, Israel, for providing the MAFA-specific mAb G63. This work was supported in part by NSF grants MCB-9807822 and DBI-0138322 to BGB, by NIH grant HD23236 to DAR and by a postdoctoral fellowship to GCL by the Consejo Nacional de Ciencia y Tecnología (CONACYT), Mexico.

J. Song, G. M. Hagen, D. A. Roess, I. Pecht, B. G. Barisas, *Biochemistry* (2002), 41, p 881-889.

CHAPTER 3

INTERACTIONS OF THE MAST CELL FUNCTION-ASSOCIATED ANTIGEN WITH THE TYPE I FCϵ RECEPTOR

INTRODUCTION

One group of immunoreceptors, the Fc receptors, are specific for the respective Fc domains of immunoglobulin isotypes and bind them with a stoichiometry of 1:1. Binding by itself does not initiate degranulation of the cells; *clustering* of Fc receptors via the bound immunoglobulins which serve as antigen-specific, divalent adapters provides the signal leading to the above cellular response[48]. Mast cells are an important experimental system for studying the events coupling Fc receptors to cellular responses. These cells respond instantly to clustering of their type I Fcϵ receptors (FcϵRI) by secreting their granules' contents, a process which can be quantitatively monitored[49,50]. The commonly-employed and stable rat mucosal-type RBL-2H3 mast cell line has 3-6x10^5 FcϵRI per cell and these bind IgE with nanomolar affinity[51]. Clustering the FcϵRI initiates a cascade of biochemical processes leading to secretion of granule-stored mediators such as histamine[52] and the *de novo* synthesis and secretion of arachidonic acid metabolites[53] and of several cytokines [54,55]. The coupling cascade includes recruitment and activation of specific protein tyrosine kinases[56]. This in turn causes a transient increase in tyrosine phosphorylation of several cellular proteins[57,58]. Resulting activation of PLCg increases phosphatidyl inositide

hydrolysis[59] and, in turn, elevates intracellular free calcium ion concentrations and activates protein kinase C[60], finally culminating in the secretory response.

Several membrane proteins are capable of modulating the FcεRI-mediated secretory response[61-65]. One such is a membrane glycoprotein named MAst cell Function-associated Antigen or MAFA. Pecht and coworkers identified MAFA as the target of the mAb G63 which inhibits RBL-2H3 cell degranulation induced by FcεRI clustering. Although at most one MAFA is expressed for every 10 FcεRI, clustering MAFA using the specific mAb G63 inhibits by up to 80% the secretory response of 2H3 cells to subsequent FcεRI clustering[66]. The question of how such a protein, expressed in sub-stoichiometric amounts, can deliver negative signals overriding those of the aggregated FcεRI is difficult to answer. MAFA aggregation inhibits both the FcεRI-induced signaling cascade upstream of PLCg activation, namely suppressing both phosphatidylinositide phosphate hydrolysis and transient intracellular calcium elevation[66,67]. The inhibitory effect of mAb G63 requires MAFA clustering and is not due to interference with IgE-FcεRI interactions[66].

MAFA has been shown to be a glycoprotein with a molecular weight of 28 to 40 kDa when expressed as a monomer and to also exist as a disulfide-linked homodimer[66]. Expression cloning of the cDNA encoding the MAFA has shown that it contains a single open reading frame, encoding a 188 amino acids long, type II integral membrane glycoprotein[68]. The deduced 114 amino acid C-terminal (extracellular) domain displays a marked homology with the carbohydrate binding domain of calcium-dependent animal lectins including the type II FcεRI (CD23) and the natural killer cell receptors. More recently it was indeed shown to bind terminal mannose residues[69]. MAFA's 34 amino acid

cytoplasmic tail contains an SIYSTL motif, an analog of the immunoreceptor tyrosine-based inhibitory motifs (ITIM)[68]. The tyrosyl residue of the MAFA's ITIM is at least partly phosphorylated upon its clustering[68,70].

MAFA-FcεRI interactions: hypothesis and rationale for experimentation

Previous studies in other laboratories and ours suggest certain parameters of interactions between FcεRI and MAFA, the membrane localization of these species, and the linkage of these interactions to the aggregation state of the molecular species.

1. Unperturbed, non-aggregated FcεRI are dispersed within the plasma membrane[71] but, upon aggregation, are translocated into lipid rafts as has been shown by Baird's group[72].
2. The Jovin laboratory has provided the crucial demonstration of FRET between FcεRI-bound IgE and MAFA-bound intact G63 mAb and shown that this energy transfer is *not* increased upon FcεRI clustering[73]. Unfortunately, in this study, receptor interactions with *unclustered* MAFA, as probed by G63Fab, were not examined.
3. Evidence for MAFA-FcεRI association was implied by 2H3 cell degranulation apparently being triggered by bifunctional antibodies specific for FcεRI and MAFA[74]. Data analysis in this paper is based on the assumption that only aggregation of FcεRI can cause cell degranulation, whereas MAFA-FcεRI clusters are considered as inactive. In such a case the degranulation caused by bifunctional antibodies can only be explained by invoking pre-existing MAFA-FcεRI aggregates.

These results leave certain questions unresolved. In particular, there is no *direct* experimental evidence for the interaction of *unclustered* MAFA with FcεRI. Specifically, is MAFA, in the *absence* of bridging ligands like mAb G63, associated with isolated FcεRI? Is it associated with clustered FcεRI?

We may hypothesize, reasoning from the above FRET and bifunctional antibody results, that MAFA is at least partly associated with the FcεRI, irrespective of the latter's aggregation state. Such a circumstance could be tested by measuring the in-membrane motions of MAFA and the receptor. Such measurements have the advantage of being performed on intact cells under nearly physiological conditions. Rotational behavior of membrane proteins, measured by time-resolved phosphorescence anisotropy (TPA), is a sensitive reflection of molecular size since the rotational correlation time (RCT) of anisotropy decay is linearly proportional to the molecule's in-membrane volume[13]. The lateral diffusion coefficient, or diffusion constant, of membrane proteins measured by fluorescence photobleaching recovery (FPR) is a weaker , *i.e.* logarithmic, function of molecular size[13]. Therefore, if MAFA is constitutively associated with the FcεRI, then TPA and FPR measurements on the MAFA-FcεRI system should yield certain specific results, given that the receptor is present in large excess:

1. MAFA should exhibit the same apparent rotational correlation time as the FcεRI and this value should be too large for an isolated molecule of MAFA's size;
2. Aggregating the receptor into large clusters should reduce the lateral diffusion coefficients of both MAFA and the receptor;

3. Such treatment should rotationally immobilize both MAFA and the receptor, thus increasing the limiting anisotropies of both species.

We have thus performed TPA and FPR measurements to resolve the nature of interactions between FcεRI and MAFA.

MATERIALS AND METHODS

Antibodies and proteins

Monoclonal antibody G63 (IgG_1) used in the present studies was purified from hybridoma culture supernatants by chromatography on protein A-Sepharose. The mAb was eluted from the column by 0.2 M sodium citrate (pH 4.5) and collected directly in tubes containing 2M tris buffer (pH 8.2). The mAb was dialyzed against phosphate-buffered saline (1.86mM NaH_2PO_4, 8.39 mM Na_2HPO_4, 0.15M NaCl; PBS) and stored frozen at -20°C. Fab fragments of mAb G63 were prepared by digestion with papain at a 1:50 w/w ratio, in 20 mM Tris buffer (pH 8.2), containing 0.1 mM dithiothreitol and 2 mM EDTA. Digestion was carried out for 2 h at 37°C after which time iodoacetamide (10 mM) was added for 1 h at 4°C. Fc fragments and undigested antibodies were eliminated by passing the preparations twice through the protein A-Sepharose column. SDS-PAGE followed by Coomassie blue staining was used to verify that Fab preparations did not contain intact or partially digested molecules. Antibody concentrations were determined by absorbance at 280 nm. G63-$F(ab')_2$ was prepared by pepsin (2.4% w/w) digestion of intact G63 (1.35 mg/mL) in 0.1M Na citrate, pH 3.7, at 37°C for 2hr. The reaction was stopped by increasing pH to 7.0. The $F(ab')_2$ product was purified by chromatography on MAPS II Protein A agarose with the MAPS II binding buffer or on HiTrap Protein G columns. Monoclonal DNP-specific A2 rat IgE was

purified from ascitic fluid by binding to DNP-Sepharose and elution with DNP-glycine[51]. 95.3 anti-mouse IgE was purified as previously described[75]. Goat anti-mouse IgG (Fab-specific; M6898), rabbit anti-mouse IgG (M7023) goat anti-mouse IgG (Fc-specific; M2650) and goat anti-DNP IgG (D9781) antibodies were obtained from Sigma, St. Louis, MO. DNP_{11}-BSA, derivatized with an average of 11 DNP-groups per molecule, was prepared as described earlier[76].

Preparation of Antibody Conjugates

Antibodies were derivatized with erythrosin isothiocyanate (Er; Molecular Probes, Eugene, OR) using a modification of methods described by Johnson and Holborow[77]. Intact antibody or Fab or $F(ab')_2$ fragments were dissolved in PBS containing 50 mM sodium borate, pH 9.3. Er was dissolved in 50 mL DMSO and diluted with 50 mM sodium borate buffer. Er concentrations were determined spectrophotometrically at 535 nm using a molar absorptivity of 101,000 L mol^{-1} cm^{-1}. A 3-fold molar excess of Er was added to the protein solutions and the mixtures incubated at room temperature for 2 hr. The reaction was quenched with 1 M Tris and dye-derivatized proteins were separated from free dye on a Sephadex G25 column. The column eluate was extracted once with an equal volume of *n*-butanol to remove any remaining non-covalently bound dye and dialyzed against PBS for a total of 48 hr at 4°C. The molar ratios for dye-derivatized proteins and their concentration in solution were determined spectrophotometrically. The antibody preparations used in these experiments had an average of 1 to 2 mol of Er per mole of intact antibody, Fab or $F(ab')_2$ fragments. Monofunctional Cy3 and Alexa 488 were purchased from Amersham Pharmacia Biotech (Piscataway, NJ) and Molecular Probes (Eugene, OR), respectively, and used for

antibody derivatization according to Manufacturers' directions. Prior to use, all dye-derivatized proteins were centrifuged at 130,000x g for 10 min in a Beckman Airfuge (Beckman Instruments, Palo Alto, CA) to remove any protein aggregates formed during storage.

RBL-2H3 cells

Rat mucosal-type mast cells of the RBL-2H3 line were kindly provided by Dr. Reuben Siraganian of the National Institutes of Health. Cells were grown as monolayers in Eagle's minimal essential medium with Earle's salts (MEM) supplemented with 10% fetal calf serum, 2mM glutamine, and antibiotics in a humidified atmosphere with 5% CO_2 at 37°C. Cells labeled with FITC-IgE and compared cytometrically with calibrated fluorescein bead standards showed typical expression of 290,000 - 400,000 FcεRI per cell[78]. Typically, 10^7 cells in 1 mL were labeled with Er-derivatized probe for each TPA experiment. Cell labeling conditions for fluorescent or phosphorescent protein conjugates were 150 nM IgE or 30 nM G63 mAb, Fab or $(Fab')_2$ at 4°C for 1 hr. Following this, cells were washed twice by centrifugation at 300 x g for 3 min in PBS to remove unbound ligand and were deoxygenated to eliminate phosphorescence quenching by O_2. To accomplish this, pelleted cells were resuspended in deaerated PBS containing 50 mM D-glucose, 0.2 mg/mL glucose oxidase (Sigma type II-S) and 0.25 mg/mL catalase (Sigma type C-10)[25]. The sample was incubated for 5 minutes before the cells were pelleted and gently resuspended in 0.5 mL of supernatant, followed by argon purging for 15 min before measurements.

Phosphorescence measurements of MAFA-bound erythrosin-G63 mAb and its Fab fragment require particular care in cell labeling. Although G63 binds MAFA with good

affinity, $1x10^8 M^{-1}$ for the Fab fragment[51], the low expression of MAFA means that particular care must be taken in selecting labeling conditions in order to attain maximum specific binding. We measured phosphorescence signals achieved by specific and non-specific binding of mAb G63 to MAFA at various antibody concentrations. The data show that only in a narrow range of antibody concentrations is an adequate signal attributable to specific binding attained. A 30 nM concentration provided approximately 90% specific binding and a reasonable signal. This labeling concentration was used for all experiments involving intact G63 mAb or its Fab or $(Fab)'_2$ fragments. Under these conditions phosphorescence signals from G63 Fab-labeled cells were at least 10-fold above the background signal from unlabeled cells

Time-Resolved Phosphorescence Anisotropy Instrumentation and Analysis

Time-resolved phosphorescence anisotropy experiments were performed as previously described[79,80] and the latter reference provides a block diagram of the apparatus employed. Washed and deoxygenated cell samples were placed in a 5 x 5 mm Suprasil quartz cuvet mounted in a thermostated housing, typically maintained at 4°C unless otherwise specified. Excitation was by the frequency-doubled 532 nm output of a Spectra-Physics DCR-11 Nd:YAG laser operated at 10 Hz with a vertically polarized TEM 00 output of 250 mJ at the sample cuvet. Sample phosphorescence was isolated by a holographic notch filter (Kaiser Optical) , a 1M $Na_2Cr_2O_7$ solution chemical filter, a KV 550 color filter (Schott Glass Technologies, Inc., Duryea, PA) to block scattered light, a 3 mm thick RG 665 filter to eliminate delayed fluorescence and a rotating polarizer to select phosphorescence emitted with vertical $I_{\parallel}(t)$ and horizontal $I_{\perp}(t)$ polarizations. The phosphorescence signal was detected

by a thermoelectrically-cooled EMI 9816 photomultiplier tube protected from light scattered during laser pulses by a fast gating circuit[34]. The photomultiplier output was amplified by a Tektronix 476 oscilloscope and a 35 MHz bandwidth buffer amplifier and 4096 traces in each polarizer orientation averaged by a Nicolet 12/70 computer equipped with a 20 MHz, 8-bit analog-to-digital converter. Data were downloaded into a PC-compatible computer for analysis. Phosphorescence intensities $I_{\parallel}(t)$ and $I_{\perp}(t)$ were analyzed[22] to yield a phosphorescence intensity function $s(t)=I_{\parallel}(t)+2I_{\perp}(t)$ and a phosphorescence anisotropy function $r(t)=[I_{\parallel}(t)-I_{\perp}(t)]/s(t)$. The phosphorescence intensity function was fitted to a sum of six fixed exponential decays of 3, 10, 30, 100, 300 and 1000μs, respectively. To facilitate comparison of phosphorescence decay between samples, mean decay half-times were calculated from the lifetimes and amplitudes of each step. Results of the lifetime analysis were used to weigh points in a non-linear least squares fit of the anisotropy data. Anisotropy data were thus satisfactorily analyzed according to a single average exponential decay model $r(t)=r_{\infty}+(r_0-r_{\infty})\exp(-t/\phi)$ which yielded the initial anisotropy value r_0, the limiting anisotropy value r_{∞} and the rotational correlation time (RCT) ϕ as well as the statistical uncertainties in these quantities[81].

Erythrosin-conjugated antibodies bound to cell membrane proteins typically exhibit initial anisotropies of 0.04 to 0.08. These values thus reflect considerable randomization of chromophore orientation on the sub-microsecond timescale. Anisotropy is observed to decay exponentially from its initial value r_0 to a final value r_{∞}, the time constant being the rotational correlation time ϕ, a quantity proportional to the in-membrane volume of the labeled protein and sensitive enough to reveal receptor dimerization events[82]. The limiting anisotropy value

r_∞, as observed at long times, arises from restrictions to free rotation of the labeled molecule. It is therefore common to speak to r_∞ as reflecting a rotationally immobile fraction and such rotational immobilization of molecules effectively occurs whenever a protein joins an aggregate which is some 10 or more times its size. All membrane proteins also exhibit some intrinsic limiting anisotropy since they rotate uniaxially rather than freely in three dimensions.

Differences in r_0 and r_∞ values between non-treated and treated cells were compared by Student's t-test[83] as implemented for equal sample numbers[84] to evaluate the probabilities that the rotational parameters observed in untreated and control samples could have arisen by sampling a single population, *i.e.* in the absence of an effect of treatment on probe rotation. The probability of observing differences between treated and control samples in two or more treatment groups when no treatment actually has effect is simply the product of probabilities for observing the individual effects. Rotational correlation times were not compared in this way. Many of the rotational correlation times reported in this study contain quite large relative errors, yet all such distributions are bounded on the left by zero. Such distributions are thus intrinsically skewed to the right, *i.e.* in the direction of larger values, and so cannot be considered normal for statistical analysis.

Fluorescence Photobleaching Recovery Instrumentation and Analysis

Equipment and methods for FPR measurements have been published elsewhere in detail[37]. The interference fringe technique provides extraordinarily high sensitivity for measurements on sparsely-expressed membrane proteins like MAFA though determination of protein mobile fractions is somewhat more sensitive to factors like cellular

autofluorescence. The microscope photometer is based on the Zeiss Axiomat microscope equipped with a Zeiss 63x, NA 1.2, Plan Neofluar immersion fluorescence objective, a fluorescence vertical illuminator and an MP03 photometer module. Standard Zeiss filters for fluorescein and tetramethylrhodamine were used with Omega dichroic mirrors 510DRLPO2 and 540DRLPO2 for measurements involving Alexa 488 and Cy3, respectively. Measurements were performed at 23°C. A Coherent Radiation Innova 100 argon ion laser provided excitation at 488 nm for Alexa 488-conjugated proteins and at 514 nm for Cy3-conjugated proteins. The illuminated region had a $1/e^2$ radius of 17 mm with laser powers of 1.6 W in the bleaching pulse and 500 mW in the probe beam. An interferometer divided the laser beam into two equal intensity components separated by a center-to-center distance of 5.5 mm[37] giving a fringe spacing at the sample of 1.75 mm. Typical experiment run times were 15 sec pre-bleach and 25 sec post-bleach with 50 msec/pt data acquisition and a bleaching time of 800 msec. Recovery traces obtained from unlabeled cells were subtracted from labeled cell traces to correct for cellular autofluorescence. The equations defining fluorescence recovery kinetics for spot photobleaching and for fringe photobleaching of spherical samples have already been presented elsewhere in detail[37]. Unadjusted raw data were represented directly in terms of the various parameters associated with a given measurement including the pre-bleach and immediate post-bleach fluorescence levels, the percentage of fluorophores mobile on the timescale of the experiment, and an appropriate function representing the recovery kinetics in terms of a decay half-time. The parameters were evaluated directly by the Marquardt nonlinear least-squares procedure[85]. From the measured time at which fluorescence recovery is half-complete and from the known

optical parameters, the diffusion constant and the fraction of labeled molecules mobile on the experimental timescale were then evaluated.

RESULTS

FcεRI-bound IgE and MAFA-bound G-63 Fab behave similarly as unconstrained membrane proteins in time-resolved phosphorescence anisotropy experiments.

A comparison of TPA measurement results for FcεRI-bound IgE and MAFA-bound G63 Fab at 4°C is presented in Table 2 and Figure 9. Decay kinetics of the erythrosin phosphorescence intensity function are markedly multi-exponential (Table 2). Analysis shows that the largest component of IgE phosphorescence decay is that at 300 μs, but that substantial amounts of all the other components contribute to the observed decay curves. The much lower signals observed for MAFA allow some contribution from phosphorescent components of cytoplasm and this is manifested in the shorter apparent phosphorescence lifetimes observed for MAFA-bound G63 Fab probes. Nonetheless, the overall phosphorescence decay curves (data not shown) of cell-bound Er-IgE and Er-G63 Fab both appear very similar.

Parameters for anisotropy decay at 4°C are also presented in Table 2. The rotational correlation times for FcεRI-bound IgE and for MAFA-bound G-63 Fab are virtually identical at 82±17 μs (mean ± SD *not* SEM) and 79±31 μs, respectively. Rotational correlation times also decrease with increasing temperature (Figure 9 inset). For IgE this decrease is from 82 μs at 4°C to 27μs at 37°C, *i.e.* about 3-fold over this temperature range. In contrast, the initial and limiting anisotropies change very little over this range. MAFA's rotational correlation time changes similarly, from 79 μs at 4°C to 38 μs at 37°C.

Table 2: Comparison of rotational parameters of FcεRI-bound erythrosin-IgE and MAFA-bound erythrosin-G63 Fab at 4°C[a]

Species	RCT (μs)[b]	r_0[c]	r_∞[d]	Intensity[e]	Decay fractions[f] 3	10	30	100	300	1000	$t_{1/2}$ (μs)[g]	n[h]
IgE	82±17	.068±.010	.039±.010	1.6×10^6	.09	.16	.16	.17	.38	.03	44±10	23
G63 Fab	79±31	.061±.022	.047±.015	0.3×10^6	.22	.33	.18	.12	.12	.03	16±2	21

[a] All indicated uncertainties are standard deviations of independent replicate measurements.
[b] Rotational correlation time in microseconds
[c] Initial phosphorescence anisotropy
[d] Limiting, *i.e* infinite-time, phosphorescence anisotropy
[e] Relative phosphorescence intensity
[f] Fractional phosphorescence decay amplitudes for the indicated time constants (μs). The typical standard deviation of individual fractions is about .02
[g] Half-time for phosphorescence decay evaluated from fitted decay curve
[h] Number of samples examined

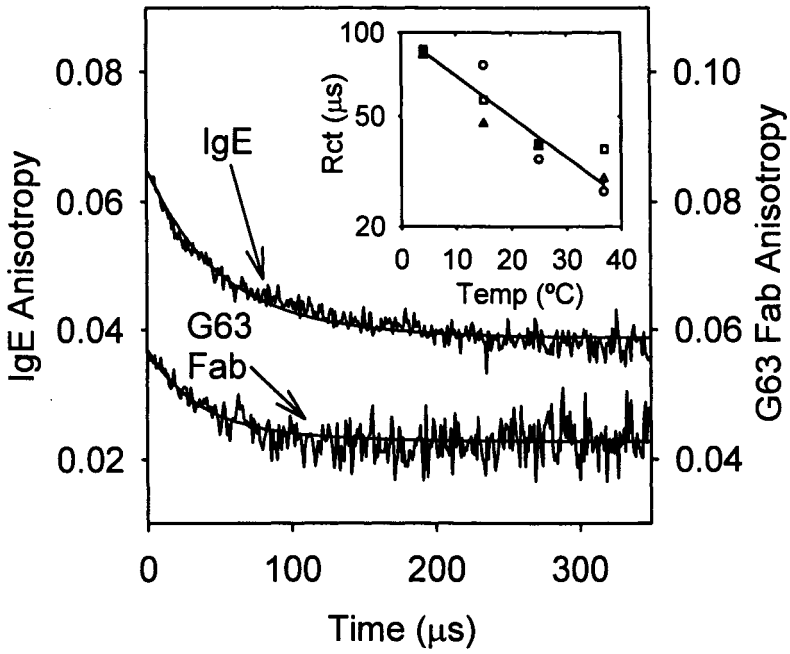

Figure 9: Anisotropy decay kinetics for Er-IgE and Er-G63 Fab bound to 2H3 cells at 4°C. Traces shown are averages of 21 experiments (IgE) and 23 experiments (G63). The inset shows the temperature dependence of rotational correlation times for the above species as well as Er-G63 intact mAb. Symbols in inset graph: O, IgE; □, G63Fab; Δ, G63 mAb. All points are satisfactorily fitted by a single curve with rotational correlation times of 84 μs at 4°C and 28 μs at 37°C. This corresponds to an activation energy of 5.9 kcal mol^{-1}, a value typical of diffusive flow in membranes.

FcεRI clustering by multivalent ligands strongly affects its membrane dynamics.

Polyvalent ligands such as antigen (DNP_{11}-BSA), which cluster the FcεRI–IgE complexes and which are thus effective in triggering mast cell degranulation, markedly affect the rotational motion of the FcεRI. For example, in one experiment, treatment with 1mg/mL DNP_{11}-BSA for 30 min at 37°C increased r_0 from 0.068 to 0.087, increased r_∞ from 0.037 to 0.058 and produced a small increase in RCT from 75 μs to 95 μs. Table 3 summarizes the effects of various treatments on FcεRI rotational dynamics. These effects were found to depend somewhat on antigen concentration when concentrations from 40 ng/mL to 70 mg/mL were used to cluster the FcεRI. Other FcεRI clustering reagents, and combinations thereof, were examined but none were more effective than antigen in restricting receptor rotational motion. MAFA was aggregated on cells binding Er-IgE by either G63 Fab or G63 $F(ab')_2$ followed in either case by second antibody, Fab-specific polyclonal goat anti-mouse IgG. Er-IgE rotation was then measured. Neither of these treatments had a discernable effect on rotation of receptor-bound Er-IgE (Table 3).

In addition, lateral diffusion of Cy3-conjugated IgE bound to variously-treated 2H3 cells was measured by interference fringe fluorescence photobleaching recovery (Table 4). Antigen treatment substantially restricted IgE lateral diffusion: The diffusion coefficient declined from 3.9±0.5 $x10^{-10}$ cm^2sec^{-1} on untreated cells to 2.8 ± 0.4 x 10^{-10} cm^2sec^{-1} after DNP_{11}-BSA treatment. By contrast, IgE diffusion coefficients measured on MAFA-oligomerized cells were 3.7±0.3 x 10^{-10} cm^2sec^{-1}, a value indistinguishable from that of untreated cells. Mobile fractions were also equivalent at 71 ± 3% and 73 ± 1 %, respectively.

Table 3: Effect of various treatments on rotation of FceRI-bound erythrosin-conjugated IgE at 4°C[a]

Treatment	r_0[b]		r_∞[c]		RCT (μs)[d]		
	treated	control	treated	control	treated	control	n[e]
DNP_{11}-BSA (1 μg/mL)[f]	.087	.068	.058	.037	96	75	1
" (10 μg/mL)[g]	.102	.064	.073	.036	93	85	1
anti-IgE[h]	.078	.067	.036	.033	85	85	1
anti-IgE+anti-IgG[i]	.086	.067	.042	.033	86	85	1
DNP_{11}-BSA+anti-IgE[j]	.096	.067	.068	.033	71	85	1
G63 Fab+anti-IgG (Fab-spec)[k]	.070±.006	.073±.005	.056±.009	.054±.012	127±74	165±83	4
G63 $F(ab')_2$+anti-IgG (Fab-spec)[l]	.078±.006	.076±.009	.063±.006	.058±.007	108±47	89±16	7

[a] Parameters for treated and control samples were obtained in the same experiment. All indicated uncertainties are standard deviations of independent replicate measurements.
[b] Initial phosphorescence anisotropy
[c] Limiting, *i.e* infinite-time, phosphorescence anisotropy
[d] Rotational correlation time in microseconds
[e] Number of separate replicate measurements
[f] DNP_{11}-BSA 1 μg/mL for 30 min at 25°C
[g] DNP_{11}-BSA 10 μg/mL for 30 min at 37°C
[h] anti-IgE 6 μg/mL for 30 min at 37°C.
[i] anti-IgE 6 μg/mL for 30 min at 37°C then rabbit anti-mouse IgG 6 μg/mL for 30 min at 37°C
[j] DNP_{11}-BSA 70 μg/mL for 60 min at 37°C then anti-IgE 6 μg/mL for 30 min at 37°C
[k] G63 Fab 30 nM for 60 min at 4°C then 14 μg/mL goat anti-mouse IgG (Fab specific) for 30 min at 37°C.
[l] G63 $(Fab')_2$ 30 nM for 1 hr at 4°C then 14 μg/mL goat anti-mouse IgG (Fab specific) for 30 min at 37°C.

Table 4: Effect of various treatments on lateral diffusion of FcεRI-bound Cy3-conjugated IgE and Alexa 488-conjugated G63 Fab at 23°C[a]

Probe	Treatment	D (10^{-10} cm^2 sec^{-1})[b]	M(%)[c]	n
IgE	none	3.9 ± 0.5	71 ± 3	10
"	DNP_{11}-BSA[d]	2.8 ± 0.4	75 ± 3	10
"	G63 mAb[e]	3.7 ± 0.3	73 ± 1	10
G63 Fab	none	2.2 ± 0.5	36 ± 3	10
"	DNP_{11}-BSA[d]	0.8 ± 0.5	36 ± 1	10
"	anti-IgG+2nd Ab[f]	0.18 ± 0.04	38 ± 1	10

[a] Measurements performed using interference fringe fluorescence photobleaching recovery. All indicated uncertainties are standard deviations of independent replicate measurements.

[b] Lateral diffusion coefficient.

[c] Mobile fraction.

[d] DNP_{11}-BSA 64 μg/mL for 30 min at 4°

[e] 30 nM G63 mAb for 1 hr at 4°C.

[f] G63 Fab 30 nM for 1hr at 4°C, goat anti-mouse IgG 14μg/mL for 1hr at 4°C and donkey anti-goat IgG 14μg/mL for 1hr at 4°C.

MAFA exhibits similar rotational behavior whether monitored by bound intact mAb G63 or by its Fab fragment

Inhibition of FcεRI -induced degranulation requires that MAFA be clustered, *e.g.* by intact mAb G63 or by its $F(ab')_2$ fragment, and thus it might be expected that either reagent would aggregate MAFA into dimers. In such a case rotation of intact G63 mAb-labeled MAFA would be appreciably slower than that of Fab-labeled MAFA. Comparison of rotational correlation times for MAFA binding Fab and mAb labels properly should include measurements in the "control" column for each ligand. When this is done, the 30 independent measurements using labeled Fab yield an average rotational correlation time of 77±28 μs while the 19 measurements using labeled mAb average 89±44 μs. This is far from the factor of 2 that might be expected but it suggests that the mAb aggregates MAFA to some extent. Moreover, both initial and limiting anisotropy values and rotational correlation times of mAb-labeled control samples resembled those of Fab-labeled samples treated with DNP_{11}-BSA. Rotational parameters of mAb-labeled samples were not greatly changed by DNP_{11}-BSA treatment.

MAFA rotation and lateral diffusion are restricted by FcεRI clustering.

A fundamental question is whether MAFA, when not aggregated, is nonetheless associated with FcεRI. We therefore measured the rotational motions of MAFA binding G63 Fab before and after FcεRI aggregation by antigen or anti-IgE. Averages of several anisotropy decay traces for MAFA rotation on cells variously treated and probed with Er-conjugated G63 Fab are shown in Figure 10. These traces show that FcεRI clustering by

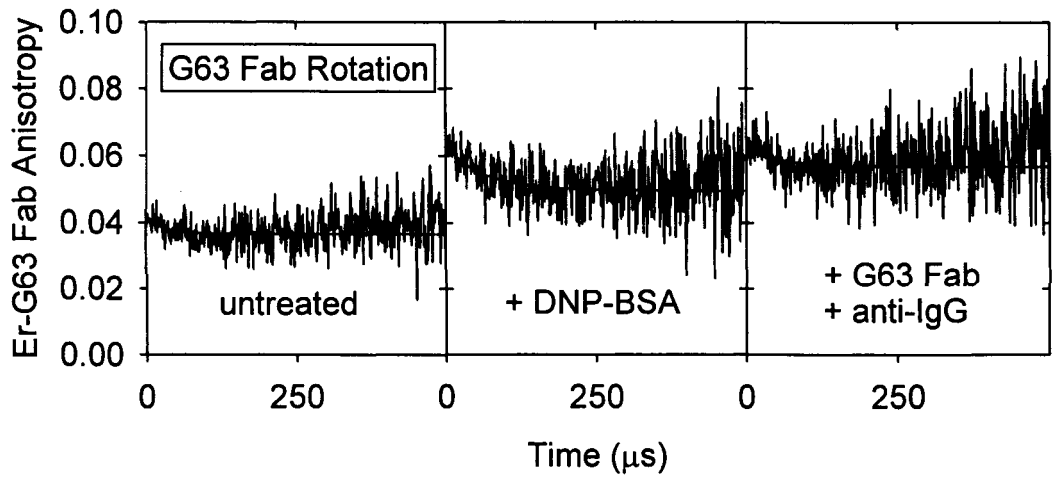

Figure 10: Effects of FcεRI and MAFA crosslinking on MAFA rotational diffusion at 4°C as probed by Er-G63 Fab. Traces shown are averages of 3-6 independent measurements. The average rotational parameters from experiments like that shown here are presented in Table 4. This table shows that FcεRI crosslinking by DNP_{11}-BSA and direct crosslinking of MAFA by G63 Fab and polyclonal anti-IgG increase MAFA rotational correlation time from 79 μs to 110 μs and 151 μs, respectively. FcεRI crosslinking by DNP_{11}-BSA produces a small but consistent increase in MAFA limiting anisotropy from 0.045 to 0.053 while direct MAFA crosslinking produces a larger increase in this quantity to 0.063. Both of these effects demonstrate restriction of MAFA rotation by either treatment.

DNP_{11}-BSA produces a substantial increase in the anisotropy of G63 Fab while aggregation of MAFA via G63 Fab and polyclonal anti-IgG produces a somewhat larger increase.

Moreover, data in Table 5 show that clustering FcεRI-IgE by DNP_{11}-BSA or by anti-IgE consistently increases the initial anisotropy, limiting anisotropy and the rotational correlation times of MAFA-bound G63 Fab. Owing to the low expression of MAFA, there are large uncertainties in these results and thus questions may arise as to their statistical significance. However, as statistical analysis shows (*c.f. Materials and Methods*), the likelihood that *all* effects on r_0 *and* r_∞ caused by DNP_{11}-BSA *and* anti-IgE treatments could have arisen accidentally is only about 1%. This strongly suggests that MAFA associates with clustered FcεRI even in the absence of MAFA clustering.

An effect of FcεRI aggregation on MAFA lateral diffusion was also observed. Clustering FcεRI by DNP_{11}-BSA reduced MAFA's diffusion coefficient from $2.2\pm0.5 \times 10^{-10}$ cm^2sec^{-1} on untreated cells to $0.8\pm0.5 \times 10^{-10}$ cm^2sec^{-1} after treatment. Figure 11 shows the visible slowing of MAFA fluorescence recovery after photobleaching on FcεRI-clustered cells. As would be expected, aggregating MAFA through G63Fab and anti-IgG produced a much larger effect on the MAFA diffusion coefficient, reducing it almost 10-fold to $0.18\pm0.04 \times 10^{-10}$ cm^2sec^{-1}. Rotation of MAFA-bound intact mAb G63 also responds to FcεRI clustering, though this is less than for the corresponding MAFA-bound Fab (Table 5). In general, anti-IgE has larger effects on rotational parameters of mAb G63 than DNP_{11}-BSA.

The Fcg domain of mAb G63 apparently interacts with additional 2H3 cell surface receptors.

Table 5: Effect of various treatments on rotation of MAFA-bound erythrosin-conjugated G63 Fab and -mAb and $(Fab')_2$ at 4°C[a]

			r_0[b]			r_∞[c]			RCT (ms)[d]	
Probe	Treatment	n	treated	control	prob[e]	treated	control	prob[e]	treated	control
G63 Fab	Untreated	21	---	.061±.022		---	.047±.015		---	79±31
	DNP_{11}-BSA[f]	6	.067±.019	.058±.024	.25	.052±.011	.045±.014	.17	110±36	73±22
	anti-IgE[g]	3	.070±.013	.057±.027	.25	.063±.017	.046±.017	.14	151±129	76±22
G63 mAb	Untreated	12	---	.060±.009		---	.051±.008		---	82±24
	DNP_{11}-BSA[f]	3	.062±.005	.063±.009	.45	.051±.004	.053±.005	.30	93±17	98±76
	anti-IgE[g]	4	.072±.004	.062±.009	.05	.062±.004	.053±.005	.02	110±75	101±58
G63 $(Fab')_2$	(vs. G63 mAb)	3	.061±.009	.065±.007	.30	.044±.006	.054±.005	.03	49±6	80±14

[a] Parameters for G63 Fab reflect representative, comparably-handled treated and control samples examined in the same experiment. For G63 mAb, untreated samples were examined as controls, treated as indicated and re-measured. All indicated uncertainties are standard deviations of independent replicate measurements.

[b] Initial phosphorescence anisotropy

[c] Limiting, *i.e* infinite-time, phosphorescence anisotropy

[d] Rotational correlation time in microseconds

[e] Probability that treated and control results could have been observed from within a single population.

[f] DNP_{11}-BSA 1-14 mg/mL for 30 min at 37°C.

[g] Anti-IgE 6 mg/mL for 30 min at 37°C.

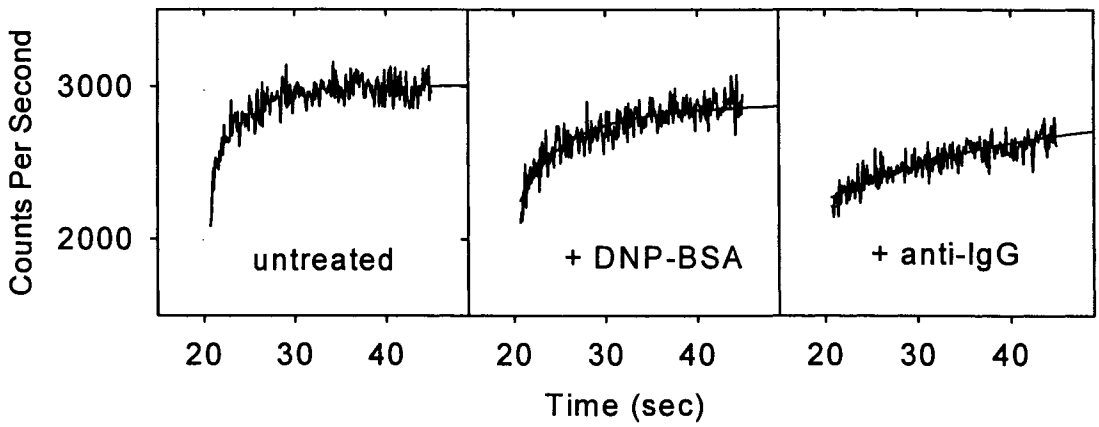

Figure 11: Effects of FcεRI and MAFA crosslinking on MAFA lateral diffusion at 23°C as probed by Er-G63 Fab. Fluorescence recovery traces shown are from a single experiment, each representing an average of 10 individual cell measurements. The y-axes of the middle and right panels have been adjusted vertically to align recovery traces. Crosslinking FcεRI by DNP_{11}-BSA reduced MAFA's diffusion coefficient from $1.90\pm0.24 \times 10^{-10}$ cm^2sec^{-1} on untreated cells to $0.76\pm0.23 \times 10^{-10}$ cm^2sec^{-1} after DNP_{11}t-BSA treatment. As would be expected, crosslinking MAFA through G63Fab and anti-IgG produced a much larger effect on the MAFA diffusion coefficient, reducing it almost 10-fold to 0.19 ± 0.03 cm^2sec^{-1}.

G63 inhibition of 2H3 cell degranulation was originally discovered as an effect of cell treatment with the intact mAb [51]. Although clustering G63 Fab was also shown to cause inhibition, we wondered nonetheless whether the Fcγ domain of this IgG_1-class antibody might also be involved in cell surface interaction, since 2H3 cells also express Fcγ receptors. We explicitly compared rotation of MAFA-bound erythrosin-G63 mAb and -G63 $F(ab')_2$ (Table 5). Three independent experiments show intact mAb G63 to exhibit higher anisotropies and a slower rotational correlation times than its $F(ab')_2$ derivative. Once again, differences are not large, but statistical analysis shows only an approximately 1% probability that both samples rotate equivalently. Moreover, differences in the rotational correlation time of the $F(ab')_2$ fragment and the intact mAb strongly suggest interaction of intact G63's Fcγ domain with a membrane entity such as FcγRII (CD32)[86].

DISCUSSION

A major issue pursued in this study is whether MAFA associates with FcεRI on non-perturbed cells. If most MAFA molecules are so associated, then they must exhibit the rotational correlation time of the unliganded FcεRI. We have therefore invested considerable effort in comparing the rotational parameters of FcεRI-bound IgE and MAFA-bound G63 Fab. Rotation of 2H3 cell bound IgE has been studied on several instances[24,78,82,87,88] and, for example, Zidovetzki *et al.* reported values in reasonable agreement with ours. There is much less information on MAFA rotational behavior[78,89]. We also found that rotational correlation times are quite consistent for each protein at a given temperature, though anisotropy values, both initial and limiting, depend somewhat upon the batch of erythrosin conjugate employed. Thus, based on our current extensive measurements, we conclude that, while it is difficult

to determine *precisely* how closely non-clustered IgE and MAFA rotational correlation times and anisotropies resemble each other, the differences, if any, seem slight.

The temperature dependence of FcεRI-bound IgE rotation has also been reported: Rotational correlation times typically fall about 3-fold as temperature is increased from 4°C to 37°C[78,87]. This is the same temperature dependence observed now both for FcεRI -bound IgE and for MAFA-bound G63 Fab (Figure 1 inset). A three-fold increase in rotation rate over this temperature range corresponds to an activation energy of 5.9 kcal mol^{-1}, a value typical for diffusive processes in membranes and one that suggests that both FcεRI and MAFA move freely in the plasma membrane, either as independent species or with MAFA associated with a fraction of the FcεRI. One can summarize that the temperature dependence of un-clustered MAFA's rotational parameters, within the considerable uncertainty of measurements on this weakly-expressed species, also appear similar to those of non-perturbed FcεRI.

The rotation of FcεRI is consistent with that expected for a 7-transmembrane segment protein. Peters and Cherry estimated an hydrodynamic diameter of 4.3±0.5 nm for bacteriorhodopsin[90] and this agrees reasonably well with the crystal structure recently published for bovine rhodopsin[91]. If one combines this value with a membrane thickness of 6.5 nm, a typical membrane viscosity of 2 Poise at 37°C and an activation energy for viscous flow of 6 kcal mol^{-1}, a rotational correlation time of about 60 μs at 4°C would be expected for a structure consisting only of the receptor's transmembrane domains. Similar calculations show that, owing to the much lower viscosity of the extracellular environment, the FcεRI extracellular domain should have essentially no effect on receptor rotation. Thus

this 60 μs value is to be compared with rotational correlation times of 82 μs measured at 4°C for FcεRI and stands in quite good agreement with them. The rotational correlation time to be expected for MAFA depends upon whether the monomer or the disulfide-linked dimer is the prevalent form. MHC Class II molecules are similar in size to the MAFA dimer and contain two transmembrane segments. Thus MAFA dimer rotation might be expected to resemble that of class II molecules. Rotational correlation times averaging 10 μs at 4°C have been measured for a number of wild-type and cytoplasmically-truncated I-A^k species[92] with somewhat slower rotation measured for I-A^d molecules[79]. Hence the rotational correlation times of FcεRI and MAFA dimers would be *expected* to differ substantially (60-80 μs *vis à vis* 10-20 μs) with a correspondingly larger difference expected for monomeric MAFA molecules. By contrast, the rotational correlation times of unperturbed FcεRI-bound IgE and MAFA-bound G63 Fab are indistinguishable (82 μs and 79 μs, respectively). Intrinsic association of MAFA with FcεRI is thus consistent with these results.

Clustering of FcεRI by multivalent ligand, whether by IgE and antigen or by polyclonal anti-IgE, markedly restricts the receptor's rotational and lateral motion. Large receptor aggregates are formed and, as Baird *et al.* have shown[93], translocated to lipid rafts. The rotational correlation time of spherical objects depends linearly upon their molecular mass[94] and, for asymmetrical objects, the dependence on size is much stronger. Large FcεRI aggregates formed by multivalent ligands thus appear immobile in microsecond-timescale rotation experiments. Such aggregation, which can also be produced by chemical crosslinking, therefore increases both the initial and limiting anisotropies of the aggregated protein[79]. However, large aggregate formation is limited kinetically by the lateral diffusion

of smaller aggregates. As aggregation proceeds, both the diffusion coefficients and concentrations of aggregates decrease so that equilibrium is never actually attained[95]. The specific rotational parameters observed are therefore functions of incubation, time, temperature and ligand concentration and valence. In our experiments, DNP_{11}-BSA treatment of FcεRI binding the DNP-specific monoclonal IgE increases both the initial and limiting IgE anisotropy and slightly prolongs the rotational correlation time. Aggregation of FcεRI by antigen thus produces the expected effects on the rotational motions of the receptor[24,96].

Restriction of FcεRI-IgE motion by anti-IgE has also been reported[87,88]. In our hands, the main effect of anti-IgE treatment is to increase IgE initial anisotropy, while further clustering with anti-IgG increases both the initial and limiting anisotropies. By contrast, it is reassuring that substantial effects of MAFA clustering on FcεRI rotation (or lateral diffusion) are *not* observed. Since unperturbed FcεRI are generally agreed to be monomeric[97] and since they outnumber MAFA by about 20 to 1 in the membrane, it is difficult to envision how FcεRI motions could be substantially affected by clustering the relatively few MAFA molecules.

Lateral diffusion of FcεRI and its ligand-induced aggregates have been previously examined using fluorescence photobleaching recovery, first by Metzger and Schlessinger[98,99] and subsequently by other investigators[100-102] as well as by other techniques[103]. Our values for the IgE lateral diffusion coefficient and mobile fraction resemble those first reported by Schlessinger *et al.*[99]. Antigen treatment of IgE-binding FcεRI seems primarily to affect the receptor diffusion coefficient rather than its mobile fraction. The Saffmann-Delbrück

treatment of diffusion in membranes shows that *lateral* diffusion depends only on the logarithm of the size of the diffusing species[13]. This logarithmic dependence suggests why simple aggregation of a membrane protein should affect only its diffusion coefficient[79]. Moreover, we showed that DNP_{11}-BSA treatment reduced the diffusion coefficient of receptor-bound IgE from $3.9x10^{-10}$ cm^2sec^{-1} on untreated cells to $2.8x10^{-10}$ cm^2sec^{-1} after DNP_{11}-BSA treatment. This actually demonstrates substantial aggregation. These numbers, together with the membrane parameters employed by Peters and Cherry[90], imply that the aggregates formed involved at least thirty-six receptors. Naturally, such large aggregates would be expected to appear immobile rotationally and, indeed, the effect of antigen treatment was to increase FcεRI limiting anisotropy while leaving the rotational correlation time essentially unchanged (Table 2).

The other major objective of the experimentation is comparison of MAFA rotation as modulated by monovalent or oligovalent ligands. In view of the experimental difficulties in monitoring the low signals produced by the Er-G63 Fab, it can only be said that these results are *consistent* with association of MAFA with FcεRI on unperturbed cells. Other types of experimental data are needed to further pursue this matter. Still, membrane dynamic data *do* permit resolution of a related question, namely whether MAFA, not itself specifically clustered, is nonetheless associated with *clustered* FcεRI. Table 2 shows effects of antigen or anti-IgE clustering of FcεRI on MAFA-bound G63 Fab rotation. Both means of aggregating FcεRI increase the limiting and initial anisotropies and rotational correlation time of G63 Fab. These data were obtained by comparing similarly treated and control samples in multiple experiments. We have already indicated that each individual effect of

FcεRI clustering is at the verge of statistical significance. However, when both treatments' effects on initial and limiting anisotropies are considered together, the probability that MAFA motion is unaffected by these treatments becomes vanishingly small. Moreover, MAFA rotational correlation times, though not analyzed statistically, also increase upon FcεRI clustering. Thus, rotation measurements clearly suggest *either* that aggregating FcεRI induces interactions between the receptor and G63 Fab-binding MAFA *or* that these interactions already exist with unclustered FcεRI. In either case, the restriction of MAFA rotation caused by FcεRI clustering would directly reflect the lower mobility of aggregated FcεRI. By contrast, the rotational diffusion parameters of MAFA when binding intact mAb G63 are virtually identical in the presence and absence of FcεRI clustering.

The data in Table 4, particularly the absence of a larger difference between the rotational correlation times of mAb- and Fab-binding MAFA, are challenging to interpret. The intrinsic problem is weak luminescence signals, a consequence of MAFA's low surface expression. These signals cause large uncertainties in measured rotational correlation times and anisotropies. Nonetheless one factor possibly limiting rotational differences between mAb- and Fab-labeled samples can be easily suggested. Only a fraction of MAFA may be associated with FcεRI (Schweitzer-Stenner *et al.*[74] estimated 60%); and, given MAFA's small size, these non-associated molecules would rotate quite rapidly. If an mAb molecule were to crosslink such an isolated MAFA with an FcεRI-associated MAFA, the complex would move in much same way as the receptor-associated species binding an Fab. In such a circumstance, mAb-labeled samples would be expected to be rotate somewhat more slowly than Fab-labeled ones, but not as much as two-fold slower. This is what is observed. We

also noted that initial and limiting anisotropy values and rotational correlation times of mAb-labeled samples were not greatly changed by DNP_{11}-BSA treatment and, in fact, resembled those of Fab-labeled samples *after* DNP-BSA treatment. This appears grossly consistent with previous results showing that the efficiency of energy transfer between MAFA-bound G63 mAb and FcεRI-bound IgE is not increased by FcεRI clustering[73]. However, an actual mechanism by which mAb binding to two MAFA molecules could have the same effects on rotational mobility as formation by DNP_{11}-BSA of large FcεRI aggregates involving MAFA is difficult to envision.

Further support for the interaction of MAFA with (at least) aggregated FcεRI comes from the lateral diffusion measurements of MAFA. Figure 11 clearly shows a slowing of MAFA's lateral diffusion upon antigen treatment, though the effect is not nearly as pronounced at that induced by direct aggregation of MAFA using G63 Fab and anti-IgG. Although though steric factors resulting from FcεRI clustering could affect MAFA diffusion indirectly, such behavior would be observed if all MAFA molecules were intrinsically associated with both isolated and aggregated FcεRI, In such a case, both MAFA lateral and rotational diffusion should consistently resemble those of its associated FcεRI so that clustering the receptor should similarly affect both FcεRI and MAFA dynamics. Certainly, the *effects* of FcεRI clustering appear similar, as do most of the dynamic parameters of the two molecules. The discrepancy in the mobile fractions of MAFA and FcεRI may be simply arise from the sensitivity of interference fringe photobleaching measurements to the accuracy of correction for cellular background autofluorescence[37].

A final issue concerns the possible involvement of the Fcγ domain of intact mAb G63 in inhibition of 2H3 cell secretory responses. In replicate experiments on comparably-handled samples we found that intact mAb G63 exhibits higher anisotropies than G63 $F(ab')_2$ and that these overall differences are highly significant. The mAb G63 is of the IgG_1 subtype[51] which has the highest affinity for the Type IIB Fcγ receptor (FcγRIIB). This receptor is known to inhibit activation signals produced by ITAM-containing receptors upon co-clustering with ITIM-containing receptors[104]. Thus, it is attractive to suppose that inhibition of the secretory response by mAb G63 might be potentiated by the interaction of its Fcγ domain with other ITIM-containing receptors also expressed on 2H3 cells, as rotational motions measurements suggest. Indeed a slight yet significantly higher inhibition of the FcεRI-induced secretory response has been observed when intact G63 mAb is used compared with its $F(ab')_2$ fragment (I. Pecht, personal communication).

Taken together, the above results support a model that is currently emerging for MAFA's inhibitory action: MAFA clustering causes a transient increase in phosphorylation of its own ITIM tyrosyl residue. The tyrosyl-phosphorylated ITIM recruits phosphatases, primarily the SH2 domain-containing phosphatase SHIP, which deplete the membranal levels of signaling phosphatidyinositol phosphates produced upon FcεRI clustering. The results presented here indicating association of MAFA with the FcεRI further support this model since the spatial proximity of MAFA to the FcεRI signaling complex would rationalize the efficacy of MAFA's action.

ACKNOWLEDGEMENTS

The Authors are most grateful to Mr. Arieh Licht for preparation of mAb G63 and other reagents used in these studies.

Adapted From: G. M. Hagen, G. Gao, D. Roess, and B. G. Barisas, *Review of Scientific Instruments, in Press.*

CHAPTER 4

IMPROVED PHOTOMULTIPLIER GATING CIRCUIT FOR TRANSIENT LUMINESCENCE EXPERIMENTS

INTRODUCTION

Many techniques in fluorescence[105,106] and phosphorescence[107-109] spectroscopy depend upon accurately recording weak emission from samples following an intense excitation pulse. When such experiments are carried out in the microsecond time range, electronic gating of the PMT is necessary to prevent gain saturation effects, artifactual anode currents, or damage to the PMT electrodes. Pulsed lasers and electrooptic modulators used in these experiments typically have rise times of a few to tens of nanoseconds. Thus the time needed for the return of normal tube operation at the end of the gate period often defines the time resolution attainable in such pulsed luminescence measurements.

Methods for the gating of PMTs include pulsing of the high voltage power supply[110], pulsing of one or more dynodes[111-114] or the photocathode[115] (PC), switching of a focusing electrode[36], or special incorporation of a gating grid[35]. A unique method termed an "optical boxcar" involved injecting a traveling high voltage pulse into a delay line so that the PMT was briefly gated on for the determination of fluorescence lifetimes. In this gate, only the light falling on the photocathode when the traveling potential is present between the PC and

dyl is amplified[116]. Selection between these methods depends on the PMT chosen, the normal operating state (on or off) and the specific experimental conditions encountered.

PMT gates are commercially available, such as the Electron Tubes Limited model GB1A. While inexpensive, small enough to fit inside a PMT base, and low powered enough to run on the voltage divider, this gate has shortcomings which precluded its use in our application. Primary among these is the 1.5 μsec rise time required for the return of normal tube bias. Another shortcoming of the GB1A is the 5V (max) gate voltage available. This is inadequate to completely eliminate very intense laser pulses used in some transient luminescence experiments where the PMT is operated at high gain.

Even when a PMT is gated so that intense laser pulses are fully extinguished, artifactual anode signals appear at the end of a gated period, as seen in figure 12. Such unwanted signals have two primary sources. Afterpulsing is due to ionization of gas within the PMT envelope and slow recombination of photoelectrons in the semiconductor photocathode. When photoelectrons are produced during PC irradiation, residual gas atoms or molecules in the PC-D1 space are ionized and accelerated back toward the photocathode with possibly a few hundred electron volts of energy. Upon impact, secondary electrons are produced and amplified by the dynode chain. This type of artifact has been extensively studied[117-121]. The work of Lee *et al.* [121] demonstrated that gaseous ions are indeed to blame for this type of artifact. The authors suggested that minimizing the potential between the PC and D1 would minimize the afterpulsing effect.

The other type of artifactual anode signal is observed only when D1 is pulsed positive such that electrons ejected from the photocathode are accelerated back toward the cathode

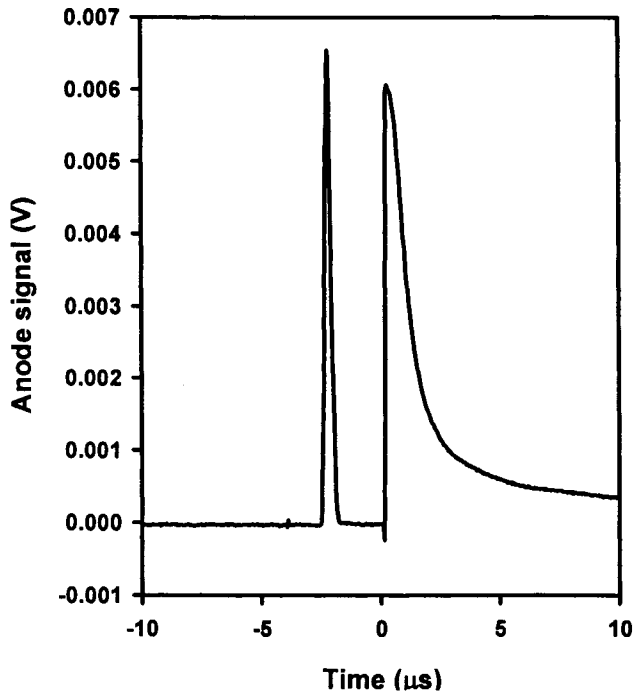

Figure 12: A microsecond afterpulse of the type encountered in this work. The digitizing oscilloscope was triggered on the gate turn-off edge. The laser pulse occurs before the gate edge, followed by a slowly decaying "afterpulse."

surface. Any photoelectrons produced during the gated period in such a system will be stored on the photocathode as they seek positive charge carriers with which to recombine. If the electrons have not recombined by the time the gated period ends, they will become free electrons and amplified by the dynode chain. Post gate artifacts in the anode current are often temporally overlapped with the signals under study, and elimination of them is generally more desirable than attempting correction.

The current gating circuit seeks to eliminate both sources of spurious gate turn-on artifacts by setting the potential between the photocathode and first dynode to an arbitrary value, usually less than the ionization potential of common gasses. Table 6 lists the first ionization potential for several gases. The gate achieves very high attenuation by further pulsing D4 and D 6. The present circuit specifically addresses elimination of light induced post gate artifacts caused by slow electron recombination times by maintaining forward bias at all times in the PC-D1 space. It also eliminates gas ion induced afterpulsing by limiting the PC-D1 potential. The small size of the previous D1/D5 gating circuit is replaced in the present implementation by an external circuit with its own power supply. The external gate has the advantage that all active elements are removed from the tube base. Emission of radio frequency signals from the high power active elements in the D1/D5 gate may have precluded its use in photon counting applications.

CIRCUIT DESIGN AND DEVELOPMENT

Our specific application involves measurement of phosphorescence lifetimes from erythrosin labeled proteins sparsely expressed on the surfaces of mammalian cells. A Lightwave model 210G Nd:YAG laser operated at 532 nm and 10 Hz - 500 Hz provides

Table 6: First Ionization Potential of Several Gasses	
H_2	15.6V
He	24.5V
O_2	12.5V
N_2	15.5V
CO_2	14.4V
Ar	15.7V
Xe	12.1V
Ne	21.5V
Kr	13.9V
CO	14.1V
H_2O	12.6V

excitation energy, usually 25 - 125μJ per pulse. Weak emission is collected in a polarization sensitive manner 90 degrees from the axis of excitation. Holographic notch, long pass, and chemical filters eliminate nearly all of the fluorescence and scattered laser light at 532 nm. Collection of phosphorescence begins one microsecond after the excitation pulse has ended.

Because of its high gain, overall ruggedness, and red sensitive S-20 spectral response, the PMT chosen for this instrument was the Electron Tubes, Inc. model 9816B. A drawback of this detector is its rather large 46 mm diameter photocathode which can produce substantial dark current. In our experiments on the microsecond timescale, dark current as great at 1000 counts per second is acceptable. The gate needed in this application must have an extinction efficiency of at least 10^4, with turn on and off times of less than 50 nsec.

The current circuit (Figures 13-18) negatively pulses D4 and D6 anywhere from 0 to 450V. It also positively pulses the photocathode anywhere from 0 to 250V. This value is set so that the PC-D1 potential will be 5-10V during the gate. In this manner forward bias is maintained in the tube front end during the gate, without ionization of residual gas. Primary photoelectrons are swept away from the photocathode and into the dynode chain. These electrons should not be able to travel past the first positively charged dynode (D4), where they are expected recombine with the metallic electrode material and become part of the ground current. Pulsing a second dynode in the manner of Ballard[111] scavenges any remaining electrons, ensuring higher overall extinction.

As in the previous gating circuit[34], a pair of complimentary power metal oxide semiconductor field effect transistors (MOSFETs) in a push pull type configuration produce the dynode 4 and 6 switching transients. The tube biasing scheme shown in Figure 13 was

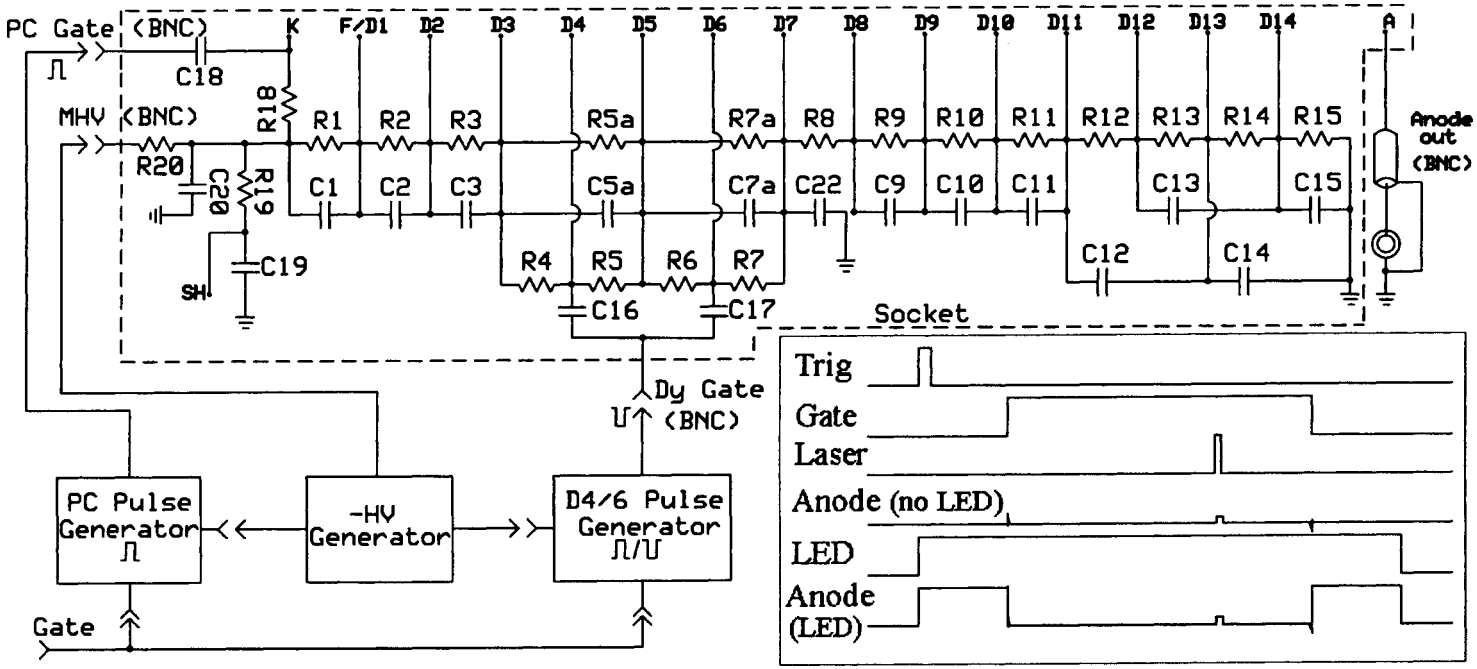

Figure 13: PMT biasing scheme with connection and timing diagrams for the photocathode/dynode 4, 6 gate.

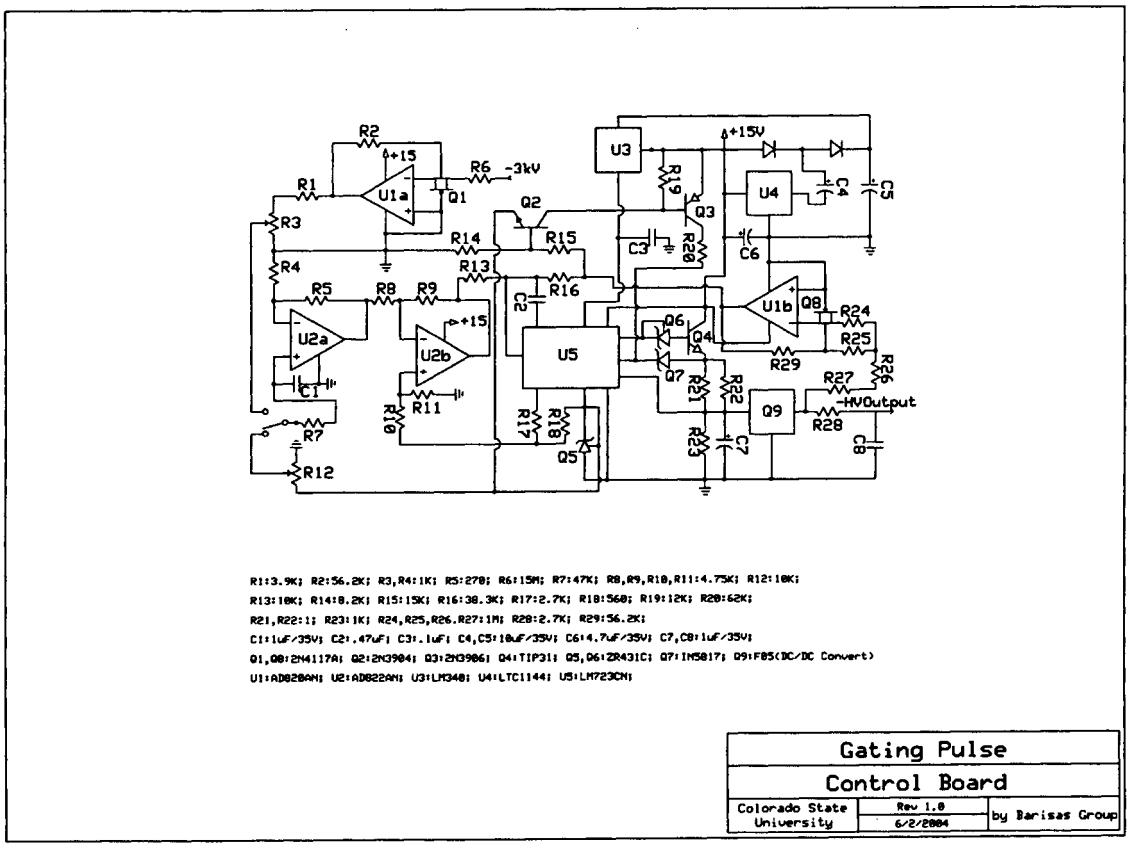

Figure 14: Control circuit for dynode 4, 6 gating pulse.

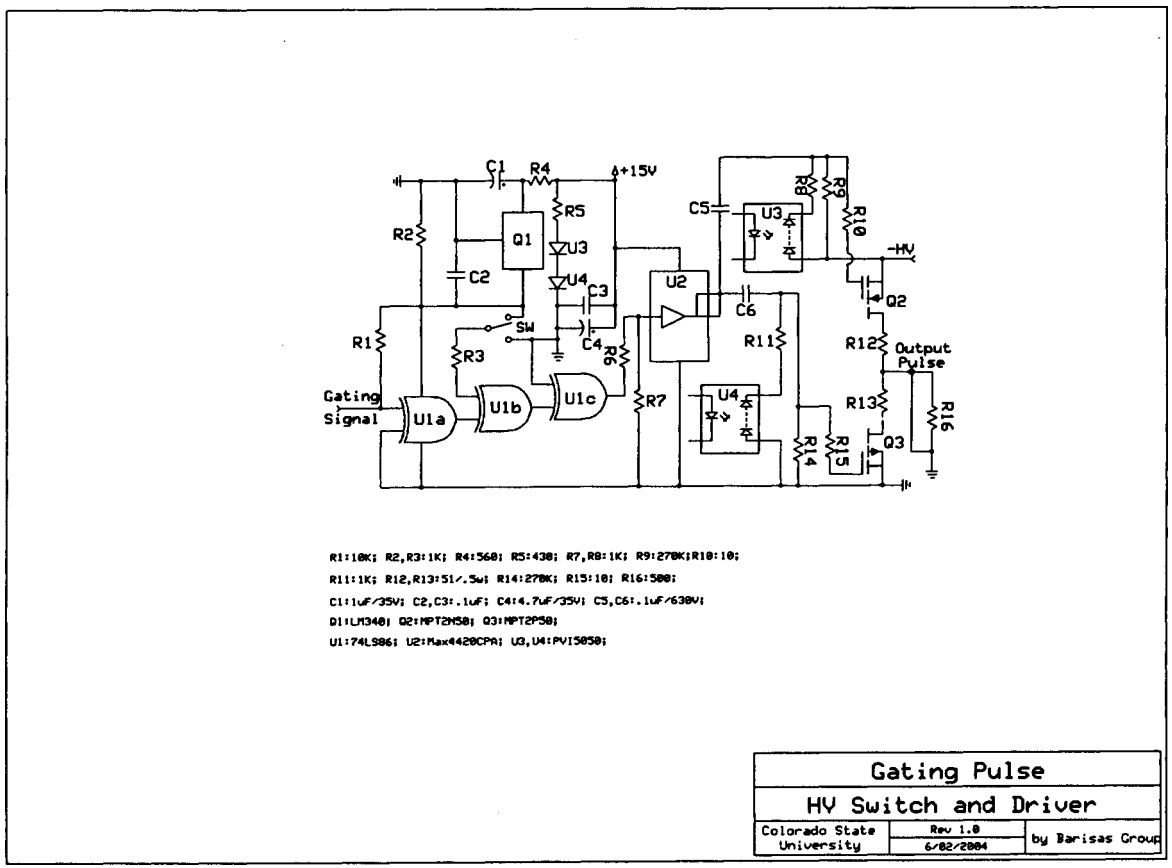

Figure 15: Dynode 4, 6 switch and driver circuit.

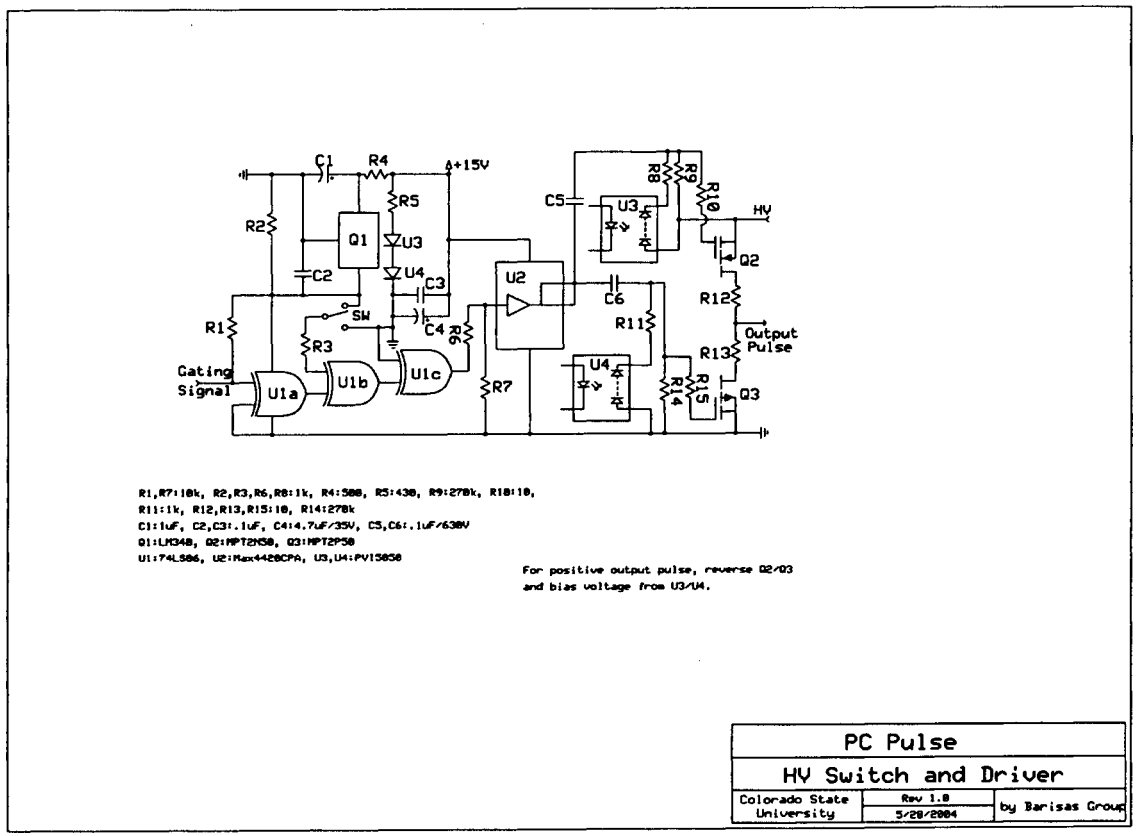

Figure 16: Photocathode pulse switch and driver circuit.

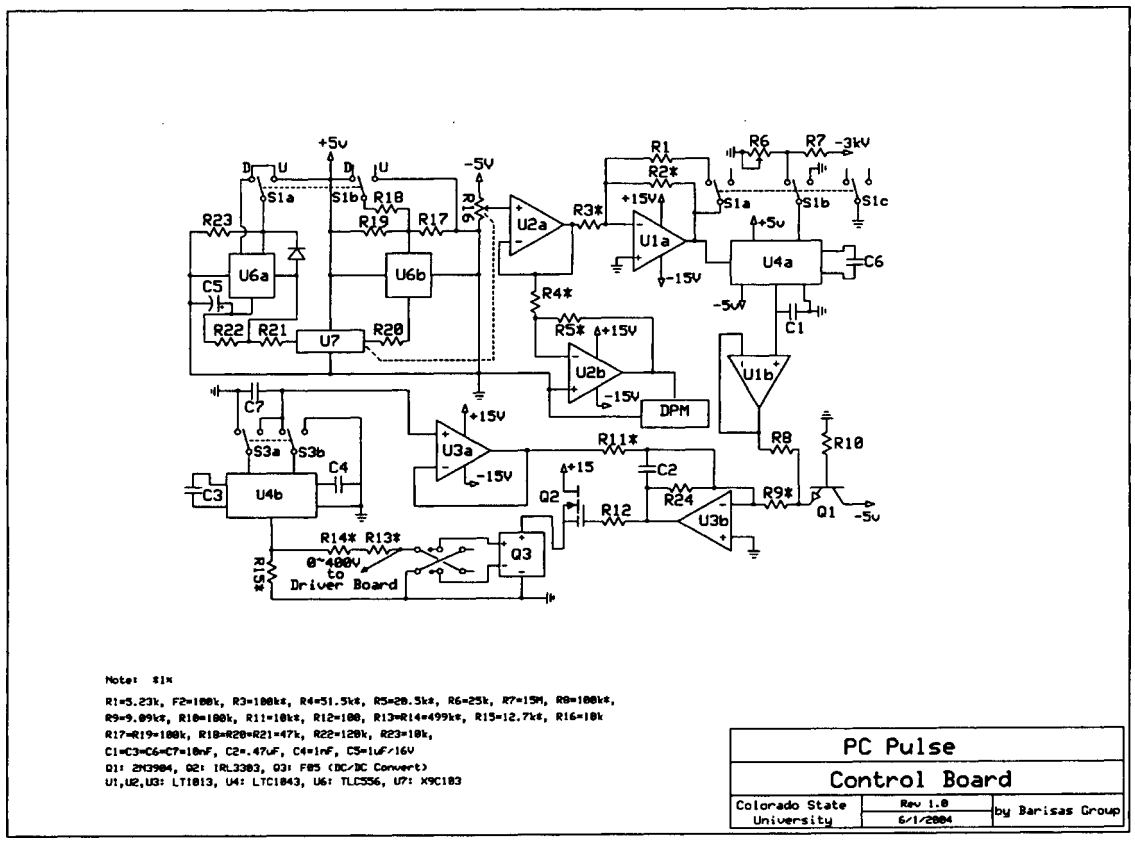

Figure 17: Photocathode pulse control circuit.

chosen so that dynodes 4 and 6 would be isolated from the rest of the divider network. This prevents the high voltage gating pulses appearing on these dynodes from coupling to the rest of the chain. Indeed, dynodes 4 and 6 are effectively removed from the amplification chain during normal tube operation. This results in a tube response which is nearly symmetrical about the gate. Connecting dynodes 11 to 13 and 12 to 14 with 0.01 μF capacitors further improved the symmetry of PMT response. The photocathode gate is built around a multifunction digital panel meter that controls the pulse voltage in both tracking and direct control modes.

RESULTS AND DISCUSSION

Pulse generators deliver desired waveforms at tube base

Figures 18 and 19 show waveforms delivered at the photocathode and at dynodes 4 and 6 by the pulse generators described above. Rise and fall times at the tube base are 20ns for both the PC and dynode generators.

Combined pulsing of PC and Dynodes 4 and 6 provides satisfactory attenuation and rise/fall times

Table 7 summarizes various operating and performance parameters of the new gate system. These are compared with the previous devices used in our laboratory for this purpose, and with a third gating strategy[122]. When the tube is operated at 1,500V, the PC-D1, D5-D4 and D6-D7 potential differences are 213V, 71V and 71V respectively. Applying a +200V pulse to the PC with no pulse on the dynodes yields an attenuation of approximately 500-fold. Similarly, a 100V pulse on D4/6 alone affords 15,000-fold attenuation. Simultaneous application of both pulses together yields over 5,000,000-fold attenuation,

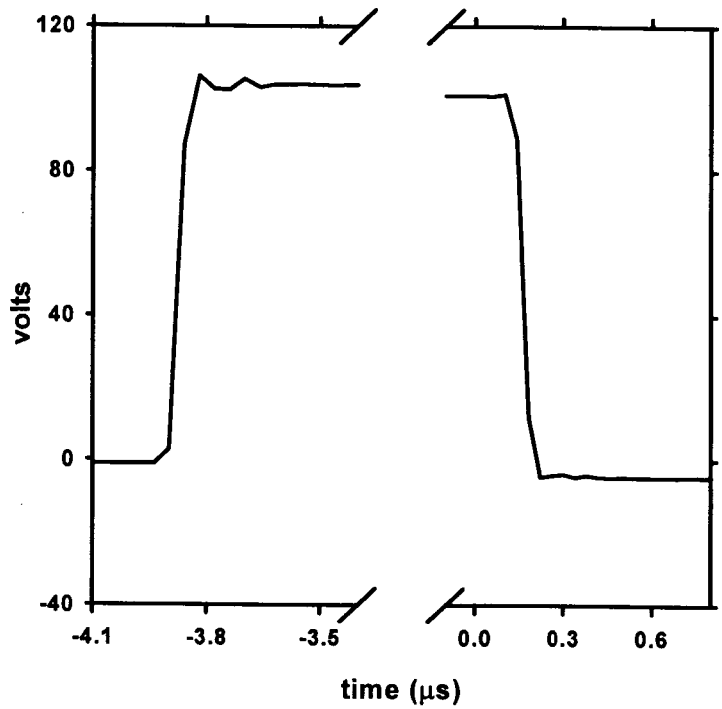

Figure 18: Shape of the positive-going pulse applied to the photocathode.

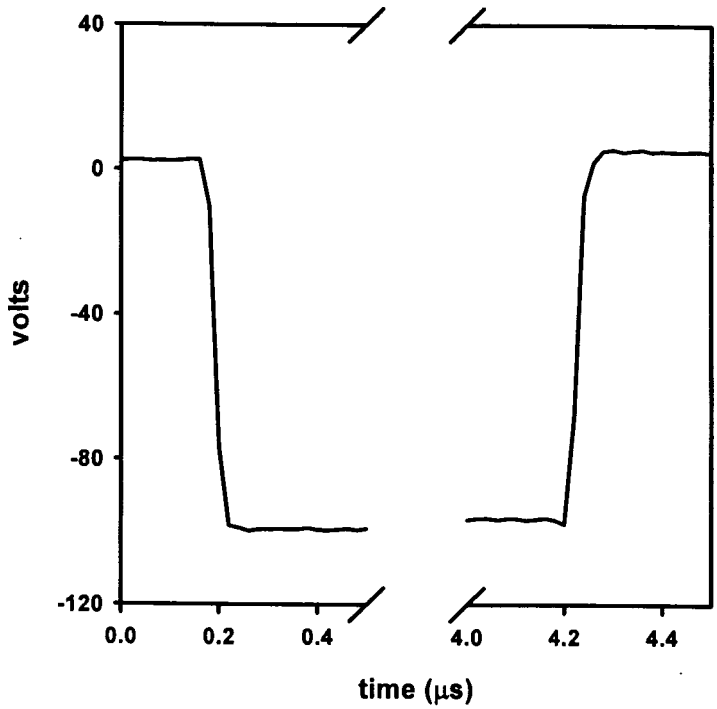

Figure 19: Shape of the negative-going pulse applied to dynodes 4 and 6.

Table 7: Comparison of PMT gating strategies

	PC, DY4,6 gate[a]	DY1,5 gate[b]	Focusing electrode gate[c]	DY 1 gate[d]
Minimum gate width	200 ns	200 ns	300ns	70 ns
Maximum gate width	0.038 ms	0.057 ms	15ms	.020 ms
Maximum repetition rate	4kHz (at GW=5 μs)	1.8 kHz (at GW=5 μs)	2.0 kHz (at GW=1 μs)	8 kHz
D1 rise time	40 ns	64 ns	150 ns	50 ns
D1 fall time	40 ns	92 ns	300 ns	20 ns
D4,6 rise time	20 ns	N/A	N/A	N/A
D4,6 fall time	20 ns	N/A	N/A	N/A
PMT turn-on time (raw)	5 ns	5 ns	‡	‡
PMT turn-on time (gated)	40 ns	40 ns	40 ns	30 ns
PMT turn-off time (gated)	40 ns	55 ns	60 ns	<50 ns
Turn on delay	220 ns	850 ns	640 ns	200 ns
Turn off delay	220 ns	300 ns	620 ns	‡
On switching transient	<3.8 mV into 50 Ω	3.0 mV into 50 Ω	1.0 mV into 50 Ω	‡
Off switching transient	<1.7 mV into 50 Ω	3.0 mV into 50 Ω	1.0 mV into 50 Ω	‡
Extinction efficiency	> $5x10^6$:1	> 10^7:1	> 10^5:1	> 10^5:1

[a] This Report.
[b] Value from Herman *et al.*, Rev. Sci. Instrum., **63**, 5454-5458 (1992).
[c] Value from Yoshida *et al.*, Rev. Sci. Instrum., **60**, 2924-2928 (1989).
[d] Value from Creasey *et al.*, Rev. Sci. Instrum., **69**, 4068-4073 (1998).
‡ No value reported.

more than adequate to eliminate scattered light signals in phosphorescence experiments (see below) and substantially more than achieved previously. Figure 20 shows the rise and fall times of gated detector response to a constant-intensity light signal from an LED. These are both 40ns.

Afterpulse magnitude varies with laser-to-gate delay

To assess the effectiveness of the gate in reducing afterpulses, an Electron Tubes 9816B PMT was mounted in a Photocool TE104RF housing with a custom base, the circuit of which is shown in Figure 13. High voltage (0 to -3000V) was provided from Bertan Model 214 supply. Laser pulses of 9 ns duration were obtained from the 532 nm frequency-doubled output of Spectra Physics DCR11 or Lightwave 210G Nd:YAG lasers. Typical pulse intensities of 250 μJ were attenuated to various lower levels by calibrated ND filters. Constant intensity light signals necessary for evaluating modulation of tube gain after a laser pulse were obtained from visible LEDs. A Berkeley Nucleonics Corporation BNC555 signal generator was used to provide repetitive sequences consisting of oscilloscope trigger, delayed gate pulse, LED drive signal (as needed) and laser Q-switch trigger (see Figure 13). Such repetitive sequences simulated conditions of intended applications and allowed signal averaging of low level signals. Signals were recorded using a Tektronix TDS744A digital oscilloscope. A Tektronix P5100 250MHz, 2500V probe was used for examination of high voltage pulses. Measurements were typically conducted at a fixed tube voltage of 1,500V and with a pulse duration of 4μs.

The Spectra Physics laser was used to deliver an optical transient 0.5 to 8.5 μsec before the end of a gated period. A dilute solution of milk was used to scatter light into the PMT

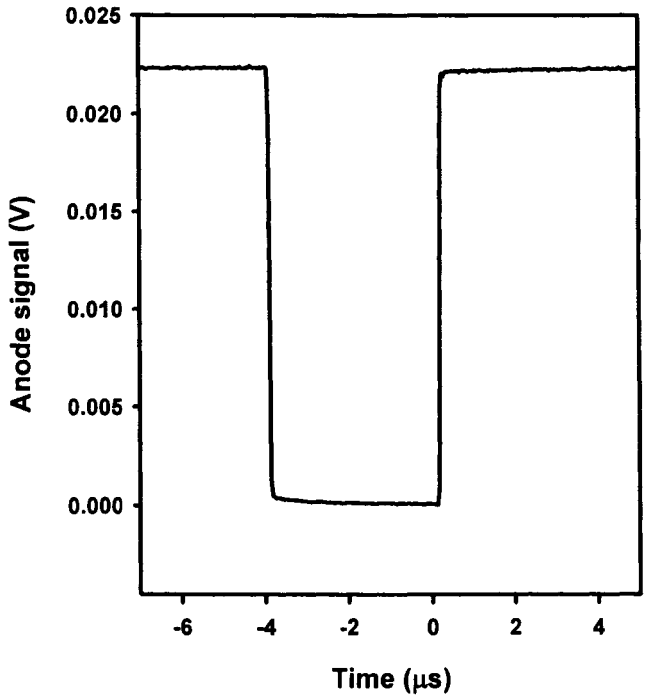

Figure 20: Gating off of the PMT during a period of constant illumination with an LED. The tube turn on and turn off times were determined from this measurement. Rise and fall times of only 20ns were measured.

after passing through a 532 nm band pass filter. As seen in Figure 21, the magnitude of the light induced post gate artifact is dependent on the position of the optical transient in the gate. This would be expected if gaseous ions were to blame for the afterpulsing observed.

To assess the role of tube gain in the level of attenuation achievable, the Nd: Yag laser was used to provide optical transients 5 μsec from the end of a 10 μsec gate. The attenuation was measured as the ratio of the anode signal arising from the laser pulse with the gate active with respect to the magnitude of the anode signal with the gate deactivated, and an OD 3 neutral density filter in place. The ratio of applied tube voltage to gating pulse voltage was kept constant at 32.0. On a log scale plot (not shown), the attenuation factor realized appeared to be linear with the tube high voltage at a constant ratio of gate voltage. This indicates the user of the gating system may vary the PMT gain over a wide range as needed without concern for gating efficiency. This feature frees the user from gate adjustment during experiments.

Limiting the photocathode-1st dynode potential to less than 10V eliminates afterpulsing.

Although initial experiments with the dynode 4 and 6 gate were promising, the gate was not capable of eliminating afterpulsing entirely. As suggested by examination of the literature,[117-121] afterpulsing might be eliminated entirely if the potential between the photocathode and first dynode could be held at 5-10V during the gate.

In most experiments on the photocathode gating circuit, a fiber optic directly coupled the attenuated laser pulses into the PMT. In these experiments, the tube voltage was -1500V and gate attenuation was nominally set to 8.5×10^4. Figure 22 shows the variation of afterpulse magnitude with photocathode pulse voltage, from 0V to 250V. With applied high

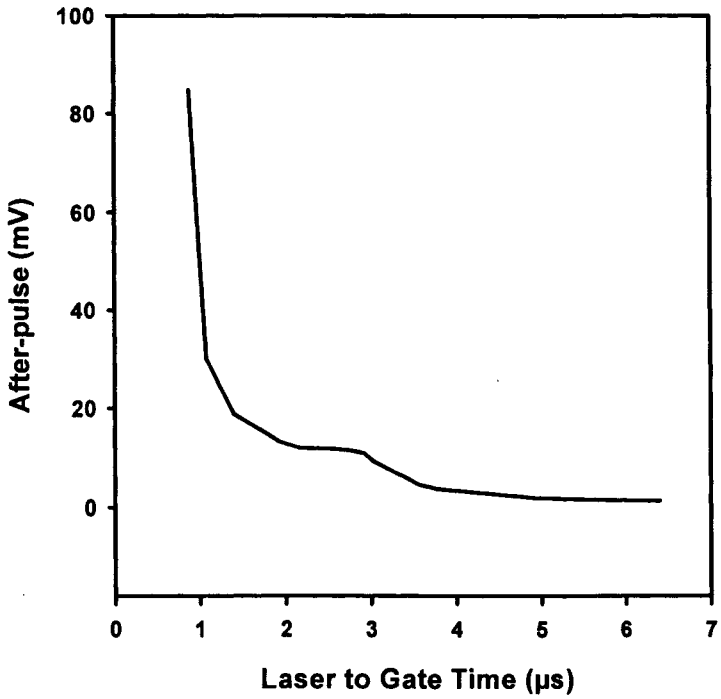

Figure 21: The size of the afterpulse increased as the laser pulse approached the gate edge.

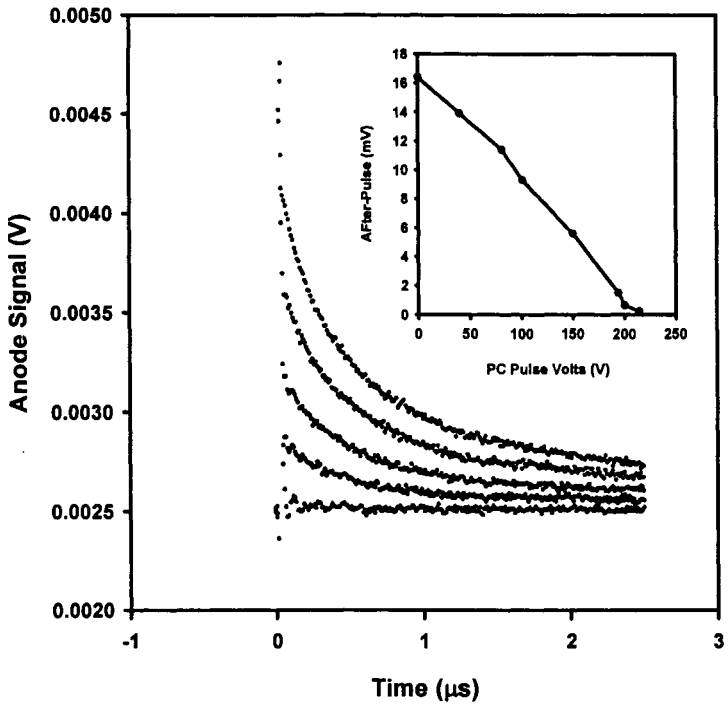

Figure 22: Variation of afterpulse size with applied photocathode pulse. Increased photocathode pulse voltages resulted in reduced afterpulsing. The inset shows the afterpulse maximum amplitude as a function of photocathode pulse voltage. Upper-most trace - no PC gate. Lower-most trace - PC gate of approximately 210V.

voltage at -1500V, the photocathode-dynode1 potential is 208V. A photocathode pulse of 202V eliminates afterpulsing. Figure 23 shows that the dynode 4, 6 gate alone has no effect on the afterpulse magnitude. This is consistent with the ion afterpulse hypothesis.

Light-induced post gates artifacts arise from even modest levels of photocathode illumination during the gate interval.

Our own application of the gating circuit involved examination of phosphorescence from suspensions of living cells. In a typical experiment, 25-125μJ of 532nm light impinged on a cuvet containing a suspension of 10^7 2H3 rat mucosal mast cells per mL. Scattered light collected by f/1 collection optics is passed through OG550 and RG665 barrier filters but nonetheless reached the PC with an energy of 0.5pJ. Some of this intensity may have arisen from luminescence of optical components. Artifacts induced by more intense laser pulses fell sharply to zero approximately 5μsec after the pulse, as would be expected from ionization-induced after pulsing. Figure 24 shows the magnitudes of the post gate signal as a function of the light pulse energy from 150pJ to 150nJ at 1μs before the gate rising edge. Clearly, such signals represent an major hindrance to measurements of luminescence on the 1-5 microsecond timescale.

CONCLUSIONS

In summary, a fast, fully adjustable, gating circuit for normally on PMTs has been developed which offers advantages over both our previous strategies[34-36] and a commercially available gate. Ion induced afterpulsing has been well documented, as noted above. Here, we describe a gating circuit capable of eliminating this type of post gate artifact. This work strongly suggests the gas ion hypothesis for afterpulse formation of this type is correct.

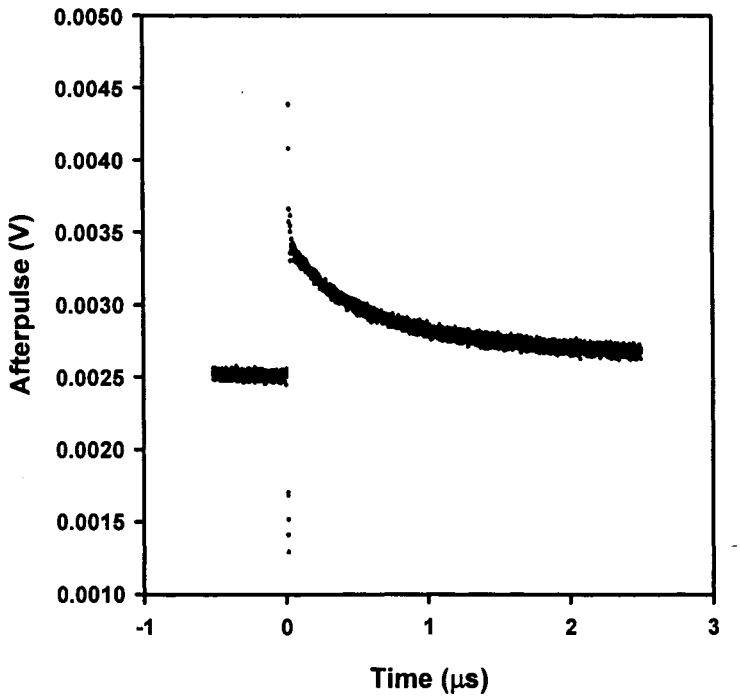

Figure 23: Afterpulse magnitude as a function of dynode 4,6 gate voltage. Several traces overlapped as the dynode 4,6 gate voltage was varied. Although effectively gating the PMT off, a 3.5mV afterpulse remained regardless of dynode 4,6 gate voltage.

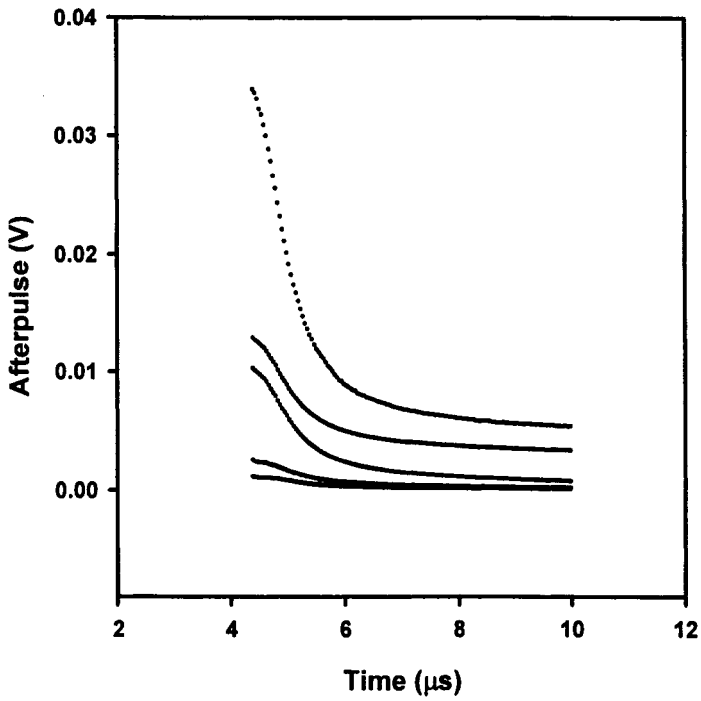

Figure 24: Even modest amounts of light produce afterpulsing. The laser pulse energy reaching the photocathode was varied from 150pJ to 150nJ, resulting in afterpulses up to 30 mV in size. Upper-most trace - 150nJ, Lower-most trace - 150pJ.

ACKNOWLEDGEMENTS

The authors wish to thank John Haase of Colorado State University for his expertise in construction and for certain elements of design of the gating circuit.

CONCLUSION OF DISSERTATION

Two new improvements to the widely used FPR technique have been realized, including for the first time combination of objective-type total internal reflection illumination with interferometric photoexcitation (TIRIF-FPR). This method extended interferometric FPR methods to be useful with VFP-expressing cells by restriction of photoexcitation to the cell membrane. Conventional spot-FPR methods with higher laser intensities have also been developed (HPI-FPR). This method allows spot-FPR measurements on cells with low levels of VFP-protein expression. New analysis procedures for HPI-FPR were also developed.

The study of the rotational and lateral dynamics of the mast cell function associated antigen (MAFA) and the high affinity receptor for IgE on the surfaces of RBL-2H3 mast cells provided biophysical evidence that the regulatory protein and receptor were coupled *in situ*. Only improved FPR techniques such as TIRIF-FPR or HI-FPR were successful in evaluating the diffusion of MAFA, since the molecule is present in extremely low quantities. Several lines of evidence from both biophysical measurements and biochemical studies suggested that the two proteins moved as a single entity in both resting and activated cells.

On-going efforts to improve time-resolved phosphorescence anisotropy methods for measurements of protein rotational diffusion required design of an efficient photomultiplier gating strategy to prevent detector damage and artifactual signals. Thus, a new photomultiplier gating circuit with high extinction and capable of eliminating microsecond

afterpulsing encountered in time-resolved phosphorescence experiments has been developed and tested. This is the fourth such gate implemented by us to resolve this problem. The results strongly support the hypothesis that afterpulsing of this type has two sources. Ionization of residual gas molecules in the space between the photocathode and first dynode led to large artifactual signals at the end of the off gated period. Charge stored on the photocathode in gating strategies that do not maintain forward bias at all times also contributed to post-gate artifacts. The new gate eliminates both sources of artifacts with a single strategy. Holding the photocathode - first dynode potential at 10V during the gated period seceded in afterpulse reduction to negligible levels, while pulsing of two intermediate dynodes provided extremely high attenuation.

REFERENCES

1. Frye, L. D. & Edidin, M. The rapid intermixing of cell surface antigens after formation of mouse-human heterokaryons. *Journal of Cell Science* **7**, 319-335 (1970).
2. Loor, F. Lectin-induced lymphocyte agglutination. An active cellular process? *Experimental Cell Research* **82**, 415-425 (1973).
3. Singer, S. J. & Nicolson, G. L. The fluid mosaic model of the structure of cell membranes. Cell membranes are viewed as two-dimensional solutions of oriented globular proteins and lipids. *Science* **175**, 720-731 (1972).
4. Poo, M.-M. & Cone, R. A. Lateral diffusion of rhodopsin in the photoreceptor membrane. *Nature* **247**, 438-441 (1974).
5. Peters, R., Peters, J., Tews, K. H. & Bahr, W. A microfluorimetric study of translational diffusion in erythrocyte membranes. *Biochimica et Biophysica Acta* **367**, 282-294 (1974).
6. Axelrod, D., Koppel, D. E., Schlessinger, J., Elson, E. & Webb, W. W. Mobility measurement by analysis of fluorescence photobleaching recovery kinetics. *Biophysical Journal* **16**, 1055-1069 (1976).
7. Jacobson, K., Wu, E. & Poste, G. Measurement of the translational mobility of con-canavalin A in glycerol-saline solutions and on the cell surface by fluorescence recovery after photobleaching. *Biochimica et Biophysica Acta* **433**, 215-222 (1976).

8. Leuther, M. D., Barisas, B. G., Peacock, J. S. & Krakauer, H. Photobleaching recovery studies of membrane events accompanying lectin stimulation of rabbit lymphocytes. *Biochemical and Biophysical Research Communications* **89**, 85- (1979).

9. Wang, Y.-L., Lanni, F., McNeil, P. L., Ware, B. R. & Taylor, D. L. Mobility of cytoplasmic and membrane-associated actin in living cells. *Proceedings of the National Academy of Science (USA)* **79**, 4660-4664 (1982).

10. Axelrod, D. Cell surface heating during fluorescence photobleaching recovery experiments. *Biophysical Journal* **18**, 129-131 (1977).

11. Jacobson, K., Hou, Y. & Wojcieszyn, J. Evidence for lack of damage during photobleaching measurements of the lateral mobility of cell surface components. *Experimental Cell Research* **116**, 179-189 (1978).

12. Koppel, D. E. & Sheetz, M. P. Fluorescence photobleaching does not alter the lateral mobility of erythrocyte membrane glycoproteins. *Nature* **293**, 159-161 (1981).

13. Saffman, P. G. & Delbrück, M. Brownian motion in biological membranes. *Proceedings of the National Academy of Science (USA)* **72**, 3111-3113 (1975).

14. Smith, B. A. & McConnell, H. M. Determination of molecular motion in membranes using periodic pattern photobleaching. *Proceedings of the National Academy of Science (USA)* **75**, 2759-2763 (1978).

15. Munnelly, H. M., Wade, W. F., Roess, D. A. & Barisas, B. G. Interferometric fringe pattern photobleaching recovery measurements interrogate entire cells. *Biophysical Journal* **70**, A447 (1996).

16. Lieto, A. M., Cush, R. C. & Thompson, N. L. Ligand-Receptor Kinetics Measured by Total Internal Reflection with Fluorescence Correlation Spectroscopy. *Biophys. J.* **85**, 3294-3302 (2003).

17. Starr, T. E. & Thompson, N. L. Total Internal Reflection with Fluorescence Correlation Spectroscopy: Combined Surface Reaction and Solution Diffusion. *Biophysical Journal* **80**, 1575-1584 (2001).

18. Thompson, N. L., Burghardt, T. P. & Axelrod, D. Measuring surface dynamics of biomolecules by total internal reflection fluorescence with photobleaching recovery or correlation spectroscopy. *Biophysical Journal* **33**, 435-454 (1981).

19. Axelrod, D., Burghardt, T. P. & Thompson, N. L. Total internal reflection fluorescence. *Annual Review of Biophysics and Bioengineering* **13**, 247-268 (1984).

20. Axelrod, D. Selective imaging of surface fluorescence with very high aperture microscope objectives. *Journal of Biomedical Optics* **6**, 6-13 (2001).

21. Bartholdi, M., Barrantes, F. J. & Jovin, T. M. Rotational molecular dynamics of the membrane-bound acetylcholine receptor revealed by phosphorescence spectroscopy. *European Journal of Biochemistry* **120**, 389-97. (1981).

22. Austin, R. H., Chan, S. S. & Jovin, T. M. Rotational diffusion of cell surface components by time-resolved phosphorescence anisotropy. *Proceedings of the National Academy of Science (USA)* **76**, 5650-5654 (1979).

23. Jovin, T., Bartholdi, M., Vaz, W. & Austin, R. H. Rotational diffusion of biological macromolecules by time-resolved delayed luminescence (phosphorescence, fluorescence) anisotropy. *Annals New York Academy of Sciences* **366**, 176-196 (1981).

24. Pecht, I., Ortega, E. & Jovin, T. M. Rotational dynamics of the Fc_ϵ receptor on mast cells monitored by specific monoclonal antibodies and IgE. *Biochemistry* **30**, 3450-3458 (1991).

25. Johnson, P. & Garland, P. B. Depolarization of fluorescence depletion. A microscopic method for measuring rotational diffusion of membrane proteins on the surface of a single cell. *FEBS Letters* **132**, 252-6. (1981).

26. Yoshida, T. M. & Barisas, B. G. Protein rotational motion in solution measured by polarized fluorescence depletion. *Biophysical Journal* **50**, 41-53 (1986).

27. Yoshida, T. M., Zarrin, F. & Barisas, B. G. Measurement of protein rotational motion using frequency domain polarized fluorescence depletion. *Biophysical Journal* **54**, 277-288 (1988).

28. Barisas, B. G., Roess, D. A., Pecht, I. & Rahman, N. A. Rotational dynamics of Fc_ϵ receptors on individual 2H3 RBL cells studied by polarized fluorescence depletion. *Biophysical Journal* **75**, 671 (1990).

29. Barisas, B. G., Rahman, N. A., Yoshida, T. M. & Roess, D. A. Rotation of plasma membrane proteins measured by polarized fluorescence depletion. *The International Society for Optical Engineering, Proceedings* **1204**, 765-774 (1990).

30. Barisas, B. G., Londo, T. R., Rahman, N. A., Herman, J. R. & Roess, D. A. Advances in polarized fluorescence depletion measurement of cell membrane protein rotation. *The International Society for Optical Engineering, Proceedings* **1432**, 52-63 (1991).

31. Barisas, B. G. & Londo, T. R. True emission and absorption anisotropies for the study of protein rotation obtained from fluorescence depletion measurements in various

experimental geometries. *The International Society for Optical Engineering, Proceedings* **1640**, 309-318 (1992).

32. Londo, T. R., Rahman, N. A., Roess, D. A. & Barisas, B. G. Fluorescence depletion measurements in various experimental geometries provide true emission and absorption anisotropies for the study of protein rotation. *Biophysical Chemistry* **48**, 241-257 (1993).
33. Barisas, B. G. & Zhang, H. Continuous fluorescence depletion anisotropy (CFDA) measurement of protein rotation. *SPIE Proceedings* **4260**, 140-148 (2001).
34. Herman, J. R., Londo, T. R., Rahman, N. A. & Barisas, B. G. Normally on photomultiplier gating circuit with reduced post-gate artifacts for use in transient luminescence measurements. *Review of Scientific Instruments* **63**, 5454-5458 (1992).
35. Barisas, B. G. & Leuther, M. D. Grid-gated photomultiplier with subnanosecond time response. *Review of Scientific Instruments* **51**, 74-78 (1980).
36. Yoshida, T., Jovin, T. & Barisas, B. A high-speed photomultiplier gating circuit for luminescence measurements. *Review of Scientific Instruments* **60**, 2924-2928 (1989).
37. Munnelly, H. M., Roess, D. A., Wade, W. F. & Barisas, B. G. Interferometric fringe fluorescence photobleaching recovery interrogates entire cell surfaces. *Biophysical Journal* **75**, 1131-1138 (1998).
38. Sako, Y., Minoghchi, S. & Yanagida, T. Single-molecule imaging of EGFR signalling on the surface of living cells. *Nature Cell Biology* **2**, 168-72 (2000).
39. Schmidt, H., Brown, E. B., Schwaller, B. & Eilers, J. Diffusional Mobility of Parvalbumin in Spiny Dendrites of Cerebellar Purkinje Neurons Quantified by Fluorescence Recovery after Photobleaching. *Biophysical Journal* **84**, 2599-2608 (2003).

40. Horvat, R. D., Nelson, S., Clay, C. M., Barisas, B. G. & Roess, D. A. Intrinsically fluorescent luteinizing hormone receptor demonstrates hormone-driven aggregation. *Biochemical and Biophysical Research Communications* **256**, 382-385 (1999).

41. Horvat, R., Roess, D., Nelson, S., Barisas, B. & Clay, C. Binding of agonist but not antagonist leads to fluorescence energy transfer between intrinsically-fluorescent gonadotropin releasing hormone receptors. *Molecular Endocrinology* **15**, 695-703 (2001).

42. Brock, R., Hammelers, I. H. L. & Jovin, T. M. Comparison of fixation protocols for adherent cultured cells applied to a gfp fusion protein of the epidermal growth factor receptor. *Cytometry* **35**, 353-362 (1999).

43. Song, J., Hagen, G., Roess, D. A., Pecht, I. & Barisas, B. G. Time-resolved phorescence anisotropy studies of the mast cell function-associated antigen and its interactions with the Type I Fcϵ receptor. *Biochemistry* **41**, 880-889 (2002).

44. Farlow, S. J. *Partial Differential Equations for Scientists and Engineers* (Dover Publications, Inc., Mineola, NY, 1982).

45. Gradshteyn, I. S. & Ryzhik, I. M. *Table of Integrals, Series, and Products* (Academic Press, New York, 1965).

46. Kaplan, W. *Ordinary Differential Equations* (Addison-Wesley, Reading, MA, 1958).

47. Brock, R., Vàmosi, G., Vereb, G. & Jovin, T. M. Rapid characterization of green fluorescent protein fusion proteins on the molecular and cellular level by fluorescence correlation microscopy. *Proceedings of the National Academy of Science (USA)* **96**, 10123-10128 (1999).

48. DeLisi, C. The biophysics of ligand-receptor interactions. *Quarterly Reviews of Biophysics* **13**, 201-230 (1980).

49. Ishizaka, T., Chang, T. H., Taggart, M. & Ishizaka, K. Histamine release from rat mast cells by antibodies against basophilic leukemia cell membrane. *The Journal of Immunology* **119**, 1589-1596 (1977).

50. Barsumian, E. L., Isersky, C., Petrino, M. G. & Siraganian, R. P. IgE-induced histamine release from rat basophilic leukemia cell lines: Isolation of releasing and nonreleasing clones. *European Journal of Immunology* **11**, 317-323 (1981).

51. Soto, E. O. & Pecht, I. A monoclonal antibody that inhibits secretion from rat basophilic leukemia cells and binds to a novel membrane component. *The Journal of Immunology* **141**, 4324-4332 (1988).

52. Schwartz, L. Mast cells: function and contents. *Current Opinions in Immunology* **6**, 91-97 (1994).

53. Ortega, E., Hazan, B., Zor, U. & Pecht, I. Mast cell stimulation by monoclonal antibodies specific for the Fcε receptor yields distinct responses of arachidonic acid and leukotriene C_4 secretion. *European Journal of Immunology* **19**, 2251-2256 (1989).

54. Bradding, P. et al. Immunolocalization of cytokines in the nasal mucosa of normal and perennial rhinitic subjects. *The Journal of Immunology* **151**, 3853-3865 (1993).

55. Galli, S. J., Gordon, J. R. & Wershil, B. K. Cytokine production by mast and basophils. [review]. *Current Opinions in Immunology* **3**, 865-872 (1991).

56. Eiseman, E. & Bolen, J. B. Engagement of the high affinity IgE receptor activates SRC protein related tyrosine kinases. *Nature* **355**, 78-80 (1992).

57. Scharenberg, A. M., Lin, S., Cuenod, B., Yamamura, H. & Kinet, J. Reconstitution of interactions between tyrosine kinases and the high affinity IgE receptor which are controlled by receptor clustering. *The EMBO Journal* **14**, 3385-3394 (1995).

58. Benhamou, M., Gutkind, J. S., Robbins, K. C. & Siraganian, R. P. Tyrosine phosphorylation coupled to IgE receptor-mediated signal transduction and histamine release. *Proceedings of the National Academy of Science (USA)* **87**, 5327-5330 (1990).

59. Beaven, M., Moore, J., Smith, G., Hesketh, T. & Metcalfe, J. The calcium signal and phosphatidylinositol breakdown in 2H3 cells. *Journal of Biological Chemistry* **259**, 7137-7142 (1984).

60. Sagi-Eisenberg, R., Lieman, H. & Pecht, I. Protein kinase C regulation of the receptor-coupled calcium signal in histamine-secreting rat basophilic leukaemia cells. *Nature.* **313**, 59-60 (1985).

61. Guo, N. et al. Monoclonal antibody AA4, which inhibits binding of IgE to high affinity receptors on rat basophilic leukemia cells, binds to novel α-galactosyl derivatives of ganglioside G_{D1b}. *Journal of Biological Chemistry* **264**, 13267-13272 (1989).

62. Ortega, E., Licht, A., Biener, Y. & Pecht, I. A glycolipid-specific monoclonal antibody modulates Fcε receptor stimulation of mast cells. *Molecular Immunology* **27**, 1269-1277 (1990).

63. Stephan, V., Guo, N., Ginsburg, V. & Siraganian, R. Immunoprecipitation of membrane proteins from rat basophilic leukemia cells by the antiganglioside monoclonal antibody AA4. *The Journal of Immunology* **146**, 4271-4277 (1991).

64. Kitani, S., Berenstein, E., Mergenhagen, S., Tempst, P. & Siraganian, R. A cell surface glycoprotein of rat basophilic leukemia cells close to the high affinity IgE receptor (FcγRI). *Journal of Biological Chemistry* **266**, 1903-1909 (1991).

65. Hamawy, M., Oliver, C. & Siriganian, R. Inhibition of IgE binding to RBL-2H3 cells by a monoclonal antibody (BD6) to a surface protein other than the high affinity IgE receptor. *The Journal of Immunology* **148**, 524-531 (1992).

66. Ortega, E. & Pecht, I. A monoclonal antibody that inhibits secretion from rat basophilic leukemia cells and binds to a novel membrane component. *The Journal of Immunology* **141**, 4324-4332 (1988).

67. Guthmann, M. D., Tal, M. & Petch, I. A new member if the C-type lectin familly is a modulator of the mast cell secretory response. *International Archives of Allergy and Immunology* **107**, 82-86 (1995).

68. Guthmann, M. D., Tal, M. & Pecht, I. A secretion inhibitory signal transduction molecule on mast cells is another C-type lectin. *Proceedings of the National Academy of Science (USA)* **92**, 9397-9401 (1995).

69. Binsack, R. & Pecht, I. The mast cell function-associated antigen exhibits saccharide binding capacity. *European Journal of Immunology* **27**, 2557-2561 (1997).

70. Rong, X. & Pecht, I. Clustering the mast cell function-associated antigen (MAFA) induces tyrosyl phosphorylation of the Fc epsilon RI-beta subunit. *Immunology Letters* **54**, 105-108 (1996).

71. Kubitscheck, U. et al. Fluorescence resonance energy transfer on single living cells: Application to binding of monovalent haptens to cell-bound immunoglobulin E. *Biophysical Journal* **60**, 307-318 (1991).

72. Field, K. A., Holowka, D. & Baird, B. Fc-epsilon-RI-mediated recruitment of p53/56lyn to detergent-resistant membrane domains accompanies cellular signaling. *Proceedings of the National Academy of Science (USA)* **92**, 9201-9205 (1995).

73. Jurgens, L., Arndt-Jovin, D., Pecht, I. & Jovin, T. M. Proximity relationships between the type I receptor for Fcϵ (FcϵRI) and the mast cell function-associated antigen (MAFA) studied by donor photobleaching fluorescence resonance energy transfer microscopy. *European Journal of Immunology* **26**, 84-91 (1996).

74. Schweitzer-Stenner, R., Engelke, M., Licht, A, Pecht, I. Mast cell stimulation by co-clustering the type I Fcϵ receptors with mast cell function associated antigens. *Immunology Letters* **68**, 71-78 (1999).

75. Baniyash, M. & Eshhar, Z. Inhibition of IgE binding to mast cells and basophils by monoclonal antibodies to murine IgE. *European Journal of Immunology* **14**, 799-807 (1984).

76. Carsten, M. E. & Eisen, H. N. The interaction of dinitrobenzene derivatives with bovine serum albumin. *Journal of the American Chemical Society* **75**, 4451-4456 (1953).

77. Johnson, G. D. & Holborow, E. J. in *Handbook of Experimental Immunology* (ed. Weir, D. M.) 28.1-28.21 (Blackwell Scientific Publications, Boston, 1986).

78. Peng, H. & Barisas, B. G. Saturation effects on phosphorescence anisotropy measurements at high laser pulse energies. *Journal of Fluorescence* **7**, 139-145 (1997).

79. Barisas, B. G., Wade, W. F., Jovin, T. M., Arndt-Jovin, D. & Roess, D. A. Dynamics of molecules involved in antigen presentation: effects of fixation. *Molecular Immunology* **36**, 701-8. (1999).

80. Philpott, C. J., Rahman, N. A., Kenny, N., Barisas, B. G. & Roess, D. A. Rotational dynamics of luteinizing hormone receptors on bovine and ovine luteal cell plasma membranes. *Biology of Reproduction* **53**, 645-650 (1995).

81. Bevington, P. R. *Data reduction and error analysis for the physical sciences* (McGraw Hill Book Company, New York, 1969).

82. Rahman, N. A., Pecht, I., Roess, D. A. & Barisas, B. G. Rotational dynamics of Fc receptors on individually-selected rat mast cells studied by polarized fluorescence depletion. *Biophysical Journal* **161**, 334-361 (1992).

83. Student. On the error of counting with a haemocytometer. *Biometrika* **5**, 351-360 (1907).

84. Sokal, R. P. & Rohlf, F. J. *Introduction to biostatics* (W.H. Freeman and Co., San Francisco, 1969).

85. Marquardt, D. W. An algorithm for least-squares estimation of nonlinear parameters. *Journal of Social and Industrial Applied Mathematics* **11**, 431-441 (1963).

86. Bocek, P., Jr., Draberova, L., Draber, P. & Pecht, I. Characterization of Fc gamma receptors on rat mucosal mast cells using a mutant Fc epsilon RI-deficient rat basophilic leukemia line. *European Journal of Immunology* **25**, 2948-55. (1995).

87. Zidovetzki, R., Bartholdi, M., Arndt-Jovin, D. & Jovin, T. Rotational dynamics of the Fc receptor for immunoglobulin E on histamine-releasing rat basophilic leukemia cells. *Biochemistry* **25**, 4397-4401 (1986).

88. Myers, J. N., Holowka, D. & Baird, B. Rotational motion of monomeric and dimeric immunoglobulin E-receptor complexes. *Biochemistry* **31**, 567-575 (1992).

89. Soto, E. O. (Weizmann Institue of Science, Rehovot, Israel, 1990).

90. Peters, R. & Cherry, R. J. Lateral and rotational diffusion of bacteriorhodopsin in lipid bilayers: Experimental test of the Saffman-Delbrück equations. *Proceedings of the National Academy of Science (USA)* **79**, 4317-4321 (1982).

91. Palczewski, K. et al. Crystal structure of rhodopsin: a G protein-coupled receptor. *Science* **289**, 739-745 (2000).

92. Munnelly, H. M. et al. Rotational and lateral dynamics of I-A(k) molecules expressing cytoplasmic truncations. *International Immunology* **12**, 1319-28. (2000).

93. Field, K. A., Holowka, D. & Baird, B. Compartmentalized activation of the high affinity immunoglobulin E receptor within membrane domains. *Journal of biological chemistry* **272**, 4276-80 (1997).

94. Cantor, C. R. & Schimmel, P. R. in *Biophysical Chemistry II* (ed. Freeman) 441 (San Francisco, 1980).

95. DeLisi, C. & Perelson, A. The kinetics of aggregation phenomena I. minimal models for patch formation on lymphocyte membranes. *Journal of Theoretical Biology* **62**, 159-210 (1976).

96. Rahman, N. A., Pecht, I., Roess, D. A. & Barisas, B. G. Rotational dynamics of type I Fcϵ receptors on individually-selected rat mast cells studied by polarized fluorescence depletion. *Biophysical Journal* **61**, 334-346 (1992).

97. Kubitscheck, U., Schweitzer-Stenner, R., Arndt-Jovin, D. J., Jovin, T. M. & Pecht, I. Distribution of type I Fcϵ-receptors on the surface of mast cells probed by fluorescence resonance energy transfer. *Biophysical Journal* **64**, 110-120 (1993).

98. Mendoza, G. & Metzger, H. Distribution and valency of receptor for IgE on rodent mast cells and related tumour cells. *Nature* **264**, 548-50. (1976).

99. Schlessinger, J., Webb, W. W., Elson, E. L. & Metzger, H. Lateral motion and valence of Fc receptors on rat peritoneal mast cells. *Nature* **264**, 550-552 (1976).

100. Menon, A. K., Holowka, D., Webb, W. W. & Baird, B. Clustering, mobility, and triggering activity of small oligomers of immunoglobulin E on rat basophilic leukemia cells. *Journal of Cell Biology* **102**, 534-540 (1986).

101. Menon, A., Holowka, D., Webb, W. & Baird, B. Cross-linking of receptor-bound IgE to aggregates larger than dimers leads to rapid immobilization. *Journal of Cell Biology* **102**, 541-550 (1986).

102. Goldstein, B. et al. Competition between solution and cell surface receptors for ligand. Dissociation of hapten bound to surface antibody in the presence of solution antibody. *Biophysical Journal* **56**, 955-966 (1989).

103. McCloskey, M. A., Liu, Z.-Y. & Poo, M.-M. Lateral electromigration and diffusion of Fcϵ receptors on rat basophilic leukemia cells: Effects of IgE binding. *Journal of Cell Biology* **99**, 778-787 (1984).

104. Daeron, M. Fc receptor biology. *Annual Review of Immunology* **15**, 203-234 (1997).

105. Velez, M. & Axelrod, D. Polarized fluorescence photobleaching recovery for measuring rotational diffusion in solutions and membranes. *Biophysical Journal* **53**, 575-591 (1988).

106. Seltzer, M. D., Hendrick, M. S. & Michel, R. G. Photomultiplier gating for improved detection in laser-excited atomic fluorescence spectrometry. *Analytical Chemistry* **57**, 1096-1100 (1985).

107. Song, J., Hagen, G. M., Roess, D. A., Pecht, I. & Barisas, B. G. The mast cell function-associated antigen and its interactions with the type I Fc-epsilon receptor. *Biochemistry.* **41**, 881-9 (2002).

108. Jovin, T. M. & Vaz, W. L. C. Rotational and translational diffusion in membranes measured by fluorescence and phosphorescence methods. *Methods in Enzymology* **172**, 471-513 (1989).

109. Piton, M. C., Panning, W. & Winnik, M. A. An "On"-gated photomultiplier circuit for the determination of phosphorescence lifetimes. *Review of Scientific Instruments* **61**, 3726-3728 (1990).

110. Singer, S., Neher, L. K. & Ruehle, R. A. Pulsed photomultipliers for fast scintillation counting. *Review of Scientific Instruments* **27**, 40-43 (1956).

111. Ballard, S. G. Normally on fast-gain switch for photomultiplier tubes. *Review of Scientific Instruments* **54**, 1473-1475 (1983).

112. Bennett, R. G. Instrument to Measure Fluorescence Lifetimes in the Millimicrosecond Region. *Review of Scientific Instruments* **31**, 1275-1279 (1960).

113. Minami, S. & Nishikawa, K. A signal sampling photomultiplier circuit. *Applied Optics* **5**, 173-174 (1966).

114. Yamashita, M. Photomultiplier gate with gating times larger than a few microseconds. *Review of Scientific Instruments* **45**, 956-957 (1974).

115. Farinelli, U. & Malvano, R. Pulsing of Photomultipliers. *Review of Scientific Instruments* **29**, 699-701 (1958).

116. James, D. R. & Siemiarczuk, A. Stroboscopic optical boxcar technique for the determination of fluorescence lifetimes. *Review of Scientific Instruments* **63**, 1710-6 (1992).

117. Torre, S., Antonioli, T. & Benetti, P. Study of afterpulse effects in photomultipliers. *Review of Scientific Instruments* **54**, 1777-80 (1983).

118. Bartlett, D. F., Duncan, A. L. & Elliott, J. R. Afterpulses in a photomultiplier tube poisoned with helium. *Review of Scientific Instruments* **52**, 265-7 (1981).

119. Campbell, L. Afterpulse measurement and correction. *Review of Scientific Instruments* **63**, 5794-8 (1992).

120. Burstyn, H. C. Afterpulsing effects in photon correlation experiments. *Review of Scientific Instruments* **51**, 1431-3 (1980).

121. Lee, H. S., Schwemmer, G. K., Korb, C. L., Combrowski, M. & Prasad, C. Gated photomultiplier response characterization for DIAL measurements. *Applied Optics* **29**, 3303-3315 (1990).

122. Creasey, D. J., Halford-Maw, P. A., Heard, D. E., Spence, J. E. & Whitaker, B. J. Fast Photomultiplier Tube Gating System for Photon Counting Applications. *Review of Scientific Instruments* **69**, 4068-4073 (1998).

LIST OF ABBREVIATIONS

ADC	Analog-to-digital Converter
BSA	Bovine Serum Albumin
CCD	Charge-coupled Device
CD	Cluster of Differentiation Antigen
CHO	Chinese Hamster Ovary
CPS	Photon Counts Per Second
D	Diffusion Coefficient
Da	Dalton (molecular weight)
DMEM	Dubelco's Modified Minimal Essential Medium
DMSO	Dimethyl Sulfoxide
DNP	Dinitorophenyl
DY, Dy, dy, or D	Dynode
EDTA	Ethylenediamine tetraacetate
EGFR or erbB1	Epidermal Growth Factor Receptor
Er	Erythrosin
eV	Electron Volt
Fab	Fraction Antigen Binding
$F(ab')_2$	Fab Prime-2 (Fab dimer)
FBS	Fetal Bovine Serum
Fc	Crystalizing Fraction of of IgG
FcεRI	High Affinity Receptor for IgE

FCS	Fluorescence Correlation Spectroscopy
FITC	Fluorescein Isothiocyanate
FPR	Fluorescence Photobleaching Recovery
FRAP	Fluorescence Recovery After Photobleaching
FRET	Fluorescence Resonance Energy Transfer
GFP	Green Fluorescent Protein
GnRHR	Gonadotropin Releasing Hormone Receptor
GW	Gate Width
HPI-FPR	High Probe Intensity Fluorescence Photobleaching Recovery
HV	High Voltage
Hz	Hertz
$I\text{-}A^k$, $I\text{-}A^d$, etc.	Nomenclature used for MHC Class II Molecules from Mouse
IF-FPR	Interference Fringe Fluorescence Photobleaching Recovery
IgE	Immunoglobulin E
IgG	Immunoglobulin G
ITAM	Immunoreceptor Tyrosine-based Activation Motif
ITIM	Immunoreceptor Tyrosine-based Inhibitory Motif
J	Joule
LED	Light Emitting Diode
LHR	Luteinizing Hormone Receptor
LIPGA	Light-induced Post Gate Artifact (afterpulse)
M%	Mobile Fraction

mAb	Monoclonal Antibody (intact)
MAFA	Mast Cell Function-associated Antigen
MEM	Minimal Essential Medium
MHC	Major Histocompatability Complex
MOSFET	Metal Oxide Semiconductor Field Effect Transistor
NA	Numerical Aperture
Nd:YAG	Neodymium Yttrium Aluminum Garnet
OD	Optical Density
PAGE	Polyacrylamide Gel Electrophoresis
PBS	Phosphate-buffered Saline
PC	Photocathode
PFD	Polarized Fluorescence Depletion (Fluorescence Depletion Anisotropy)
PMT	Photomultiplier Tube
PLCg	Phospholipase C Gama
RCT	Rotational Correlation Time
RBL	Rat Basophilic Leukemia
SEM	Standard Error of the Mean
SD	Standard Deviation
SDS	Sodium Dodecylsulfate
SHIP	SH_2 domain-containing Inositol Phosphatase
TEM	Transverse Electromagnetic Mode
TIR	Total Internal Reflection
TIRIF-FPR	Total Internal Reflection Interference Fringe Fluorescence Photobleaching Recovery

TPA	Time-resolved Phosphorescence Anisotropy
TRIS	Tris Hydroxymethylaminoethane
V	Volt
VFP	Visible Fluorescent Protein